Available online at www.sciencedirect.com
SCIENCE DIRECT
Polymer 47 (2006) 5371–5391
polymer
www.elsevier.com/locate/polymer

Nanoparticle induced network self-assembly in polymer–carbon black composites

Y. Konishi, M. Cakmak *

Polymer Engineering Institute, University of Akron, Akron, OH 44325, USA

Received 15 November 2005; received in revised form 6 May 2006; accepted 8 May 2006
Available online 19 June 2006

Abstract

A novel percolation phenomenon with inorganic nanoparticle loading in polyamide 6-carbon based nanoparticle hybrids was identified. Percolation threshold substantially shifts to lower carbon black (CB) volume fractions in the presence of optimum concentration of chemically modified montmorillonite (organoclay) while the effective organoclay concentration can be optimized to lower the slope of percolation curve maintaining electrical conductivity within static dissipative 10^{-6}–10^{-9} S cm^{-1} range. Organoclay/CB 'nano-unit' morphology was found in polyamide 6 ternary hybrids. It is composed of stacked organo-montmorillonite platelets that deform to wrap partially around one or two primary CB aggregates. This elementary nano-unit structure induces CB network self-assembly within polyamide 6 matrices. The structure was found to be prevalent throughout the polymer matrix. This morphology remains robust under wide range of thermal-deformation histories due to the strong preferred organoclay/polyamide 6/CB interactions that partially blocks the electron conduction and hopping mechanisms with clay 'walls' thereby reducing the slope of the percolation curve. Organoclay can be used as a dispersion control agent in these polymer–carbon systems to induce self-assembly of CB network at low CB content, simultaneously, partial blocking the electron hopping pathways to level the slope of percolation curves. High order exfoliation and nano-scale dispersion of organoclay is essential to induce this advanced percolation phenomenon.

Keywords: Conductive plastics; Self-assembly; Nanocomposites

1. Introduction

Electrical properties of polymer–carbon black (carbon black: CB) nanoparticle composites are greatly affected by CB properties including particle size, specific surface area, aggregate structure, and surface chemistry. Particularly, the latter influences the CB dispersion through polymer–CB interactions. Electrical conductivity of insulating polymers shows sharp non-linear increase with increasing CB volume fraction, resulting in long-range connectivity of conductive CB particles. This phenomenon is called 'percolation' and the critical CB volume fraction where this occurs is known as 'percolation threshold (V_f^*)'. These conductive composites are utilized in wide range of applications including electrostatic discharge (ESD) protection and electromagnetic radiation shielding for space, electronic, and electro-packaging applications [1,2]. The requirements for each application from these composites vary. For instance, electrical conductivity for the ESD protection needs to be controlled at intermediate values (10^{-6}–10^{-9} S/cm) that is rather difficult due to the steep slope of percolation curves at the percolating region. There is also a strong desire in almost all applications to reduce CB volume fraction from these composites to suppress contamination of sensitive electronic components that they encapsulate.

There have been extensive experimental and theoretical studies on the mechanism of percolation in isotropic polymer–CB composites. The origin of percolation theory can be traced back to Flory's theory [3] for polymer gelation; however, the first known literature on percolation theory is attributed to Hamersley et al. [4] in 1957. Although the objective of percolation theory is to define how a set of randomly positioned sites can be interconnected to each other, this concept was utilized to explain other physical and chemical phenomena including conductive two-phase systems. Gurland [5] first experimentally observed percolation in silver-filled bakelite composites and investigated the mean contact number for each silver particle in bakelite matrix with his original percolation theory in 1966. Then, Aharoni [6] experimentally showed that the conductivity is directly dependent on the surface area or the conducting

* Corresponding author.
E-mail address: cakmak1@uakron.edu (M. Cakmak).

0032-3861/$ - see front matter © 2006 Elsevier Ltd. All rights reserved.
doi:10.1016/j.polymer.2006.05.015

particles. Janzen [7] derived a model based on Gurland's experimental result [5] with Kirkpatrick [8], Zallen [9], Aharoni [6], and Gurland's theoretical results [5] by emphasizing the number of contacts that conducting particle could have with its neighbors. Bueche [10] used Flory's gelation theory [3] to explain non-linear percolation curves. The latter approach has parallels with the Kirkpatrick and Zallen's models [8,9]. There have also been geometrical and structure-oriented statistical models for description of percolation. The geometrical models [11,12] assume the sintering process and the insulating particles are deformed into regular cubic lattice wherein the conducting particles are arranged into a regular distribution on the surface of insulating particles. On the other hand, the structure-oriented models [13] consider micro-level structure of molded two-phase systems for limited processing techniques (sintering and compression molding) based on the geometry and coordination number of conductive particles in the system. These theoretical approaches [4–14] often have difficulty in describing the polymer/filler species' dependence on V_f^* and the slope of percolation curve mathematically or statistically.

The electrical percolation in polymer–CB composites is greatly influenced by the type of polymers and CB, preparation temperature and time as well as mixing methods used. For instance, the electrical percolation in polymer–CB composites is affected not only by CB geometry but also by thermodynamic effects. Some of these additional factors are: (i) affinity between CB surfaces [15,16] and (ii) flexibility of polymer chains [17,18]. Miyasaka, Sumita, Wessling, Asai, and co-workers [19–22] proposed thermodynamic models with interfacial interaction parameters between polymer–CB boundary described by interfacial excess energy and surface tensions of each component in order to explain the disagreements between the statistical models' prediction and experimental results [4–14] on V_f^*. For instance, original Miyasaka model [19] suggested that CB network formation begins when the interfacial excess energy reaches a certain universal value. Later, in modifying Miyazaka model [19], Sumita [20,21] and Asai [21] considered the electrical percolation as a non-equilibrium state. Sumita–Asai model [20,21] includes such factors as geometrical (volume, surface area, and radius of CB), structural (viscosity of polymer matrix), and kinetic (time of mixing and molding and/or annealing). There have been other thermodynamic models proposed on electrical percolation. These are reviewed by Medalia [17] and Lux [23]. It should be pointed out that isotropic electrical percolation in polymer–CB composites is a well-defined dynamic process of three-dimensional CB network formation and it is affected by a range of mechanisms [17,18,23,24]. These include: (i) polymer chain mobility in the vicinity of CB surface, (ii) specific interactions between polymer chains and CB surface, (iii) crystallization kinetics of polymer, and (iv) chain orientation and relaxation that may influence the physical conduction mechanisms such as electron tunneling (or hopping), dielectric breakdown, and internal field emission via thin polymer layers around CB.

The reduction of V_f^* can be achieved by using immiscible two-phase isotropic polymer systems, where the CB preferentially is either concentrated in one of the polymer phases or located at their interfaces. Such systems said to have 'double percolation' [25,26]. When the viscosities of two polymers are comparable, CB is located in the polymer phase with higher surface tension. Gubbels et al. [27] reported V_f^* values as low as 0.4 wt%. Feng et al. [28] and Ibarra-Gomez et al. [29] studied the double percolation in immiscible two-phase polymer systems with mismatched viscosity and found that CB is preferentially dispersed in the lower viscosity phase. Wu et al. [30] found large reduction of V_f^* in miscible binary blend systems (PMMA/PVDF) at 50/50 composition. They attribute this unusual behavior to preferential adsorption of PVDF on carbon black particles. This leads to heterogeneous distribution of CB particles leading to observed reduction in V_f^*.

V_f^* can be also reduced in a single polymer matrix by subjecting it to annealing in a molten state. Sumita, Asai, and their co-workers [31–33] extensively studied this 'dynamic percolation' mechanism. The critical time to achieve percolation is defined as 'percolation time (t_p)' and it shifts to a shorter time with the increase of interfacial tension between polymer and CB, annealing temperature, and by the reduction of polymer matrix viscosity.

Few studies focused on control of electrical properties and leveling of percolation curves by chemical modification of CB surface such as oxidation [34] and/or fluorination [35,36]. Sumita et al. [37] first found the reduction of slope on percolation curves in ethylene–vinyl acetate copolymer (EVA) above 32 wt% of vinyl acetate (VA) concentration. They attributed the leveling of percolation curves to the increase of polar groups in EVA, resulting in decrease in interfacial tension and enhancement of bonding to CB.

The control of V_f^* and leveling of percolation curves have not been extensively studied. Narkis et al. [2] reported the formation of 'triple percolation' in oriented glass fiber (GF)/ CB/ immiscible two-phase polymer systems that form multi-co-continuous networks of GF, CB, and polymer phase. The increase of polarity [38] by varying the EVA composition was found to level certain regions of percolation curves of CB/ EVA/LDPE systems leading to 'two step percolation'. This polarity enhanced leveling effect was also found by Feller et al. [39] in intercalated clay nanoparticle/polymer/CB systems. Smith et al. [1] recently combined the carbon nanotube (CNT) and inorganic salt ($CuSO_4$) into amine-terminated polyimide that resulted in reduction of V_f^* due to the increase in ionic concentration. This resulted in minimized potential energy between CNT and CNT particles leading to induced CNT network formation [40].

Recently, polymer–clay nanocomposites [41] have attracted much attention due to the unusual physical properties and morphology that are not readily available in conventional polymeric composite materials. Chemical modification on layered silicate platelet nanoparticle (organoclay) plays important role for intercalation, exfoliation, and nano-scale dispersion in polymers including nylon 6. Organoclay in nylon 6 matrix can be dispersed by two major methods: one [41,42] is

by in situ polymerization of ε-caprolactam and organoclay modified by 12-aminolauric acid or longer alkylene chain attached in amino acids as a catalyst. The other is by melt blending with nylon 6 and organoclay modified by quaternary ammonium chloride and/or by hydroxyl or carboxyl groups. The interlayer distances of organoclay increase with the diffusion/penetration of nylon 6 chains associated with mechanical shear and in amide groups of nylon 6 may be formed hydrogen bonds with the functional groups attached to the organic modifier or the amine end-groups may have physical interactions such as London (non-polar) interactions on the pristine silicate platelet surface that the interfacial tension between nylon 6/organoclay may become extremely small. However, the mechanism of nylon 6-clay (or organoclay) interactions for intercalation/exfoliation and the factors (or driving force) for organoclay nano-scale dispersion in the absence of shear flow are still unclear [43–45].

To our knowledge, the effect of organoclay-loading on electrical percolation behavior in polymer–CB composites and its morphological mechanism in both isotropic/oriented states have not been comprehensively investigated yet.

In this paper, we identify the organoclay-loading induced advanced percolation concept under fully exfoliated organoclay dispersion state in isotropic nylon 6-CB composites prepared by conventional melt blending. The techniques used to identify advanced percolation concept include: electrical, rheological, electron and electric force microscopy, and X-ray diffraction techniques. Heat of immersion measurement technique was used to quantify the contribution of interfacial energetic factors between layered silicates/nylon 6/CB associated with investigation on the mechanism of nylon 6-clay (natural clay versus organoclay) interactions on CB network formation.

2. Experimental procedures

2.1. Materials

Commercial grade neat nylon 6 (299 A X 83130 A®) and melt blended nylon 6 nanocomposites with 3 vol% (299 A X 83134 A®) and 5 vol% (299 A X 83134 B®) organoclay-loading (RTP Company, USA) were used in this study. Commercial low-structure rubber grade carbon black (CB) (Seast® G-SVH: primary particle diameter: 62 nm, N_2 specific surface area: 32 m^2/g, DBP oil absorption: 140 $cm^3/100$ g) as a conductive nanoparticle was kindly provided by Tokai Carbon Co., Japan. Two types of layered silicate nanoparticles (Southern Clay Products, USA) were employed: (i) natural montmorillonite (Cloisite® Na^+; nanoclay) and (ii) organo-montmorillonite (Cloisite® 30B; organoclay), which was chemically modified to include quaternary ammonium chloride with methyl, tallow, bis-2-hydroxyethyl in order to exchange the sodium cation between layered silicates and induce hydrophobic-like structure on the hydrophilic silicate surfaces. The organic modifier has unsaturated aliphatic chains attached with two hydroxyl groups.

2.2. Sample preparation

Neat nylon 6 and nylon 6 nanocomposites in the form of extruded pellets and as received CB in the form of fine powder were dried at 80 °C for 24 h under vacuum prior to melt blending. The melt blending was carried out by using an internal mixer (Brabender Plasticorder, USA) for 10 min at 245 °C using 60 rpm rotation speed. Isotropic films (0.5 mm thickness) and disks (2.0 mm thickness with 25.0 mm diameter) were compression-molded at 250 °C for 10 min under a pressure of 20 MPa, followed by air cooling at room temperature for 5 min. Differential scanning calorimeter (Model DSC 7®, Perkin–Elmer) was used to determine the thermal properties of isotropic molded films as shown in Table 1.

2.3. Sample sectioning procedure

The geometry of compression molded part and sectioning plane are shown in Fig. 1. Considering very mild anisotropy introduced by the compression molding process (squeezing flow), a mirror symmetry plane in a (TD–ND) plane in the center of the molded disk was selected. The ultrathin film (20–70 nm) sectioning across the thickness designated as B-cut for subsequent TEM study was performed by cryo-ultramicrotomy (Model MS1B®, Micro Star Technologies, USA) at room temperature by using a diamond knife.

2.4. Heat of immersion measurements

In order to obtain quantitative information on the effect of chemical modification of clay where different intermolecular interactions via nylon 6/CB are expected, heat of immersion was measured by using a twin conduction type isothermal microcalorimeter (Tokyo RIKO Co. Ltd, Japan). Both nanoclay and organoclay were dried at 110 °C for 24 h prior to measurements and low-molecular-weight liquids such as distilled water (bipolar), *n*-octane (pure; apolar) (Kanto chemical Co. Ltd, Japan), and formamide (purity >98%; bipolar) (Kanto chemical Co. Ltd, Japan) were used as probes for the heat of immersion measurements. Clays were sealed in

Table 1
Thermal properties of nylon 6 and nylon 6 nanocomposites

Matrices	DSC (10 °C/min; second heating/cooling			
	T_m (°C)[a]	T_c (°C)[b]	ΔH_f (J/g)[c]	X_c (%)[d]
Neat nylon 6	223	168	49.14	21
Organoclay/nylon 6 (0.03/0.97)	215/223	172	41.33	17
Organoclay/nylon 6 (0.05/0.95)	223	173	48.67	20

[a] Melting temperature.
[b] Crystallization temperature.
[c] Enthalpy of fusion of nylon 6 within the nanocomposites.
[d] Crystallinity obtained by using the ratio of $\Delta H_f/\Delta H^\circ$ where $\Delta H^\circ = 240$ J/g obtained from Ref. [87].

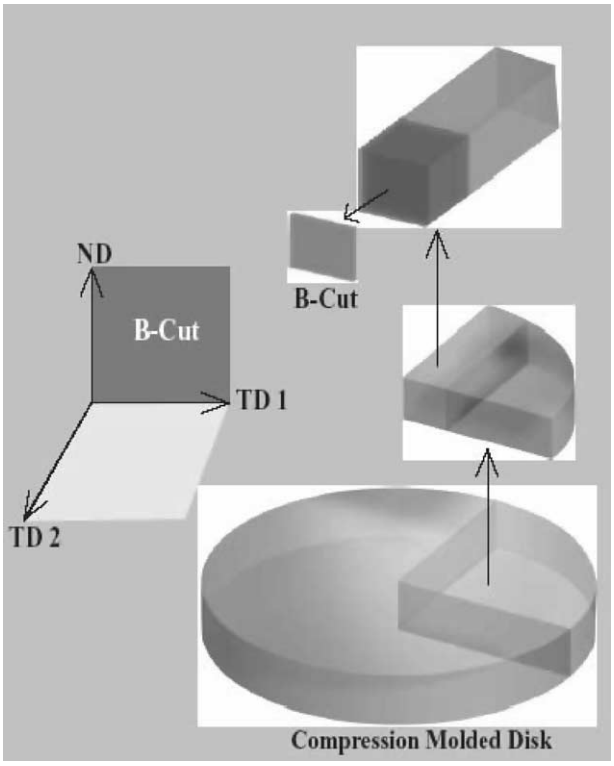

Fig. 1. Schematic of the sample sectioning procedure for TEM study.

a glass ampoule and contained in one cell; whereas, an empty ampoule was dipped in given volume of probe liquids in another cell in order to eliminate the heats generated by a breakage of the ampoule during the measurement. The probe liquids were held until they reached thermal equilibrium at 25 °C with ±1 °C accuracy. Both ampoules were simultaneously broken under atmospheric conditions and clay was immersed in the probe liquids while heat flow change as a function of time was recorded. A surface area analyzer (Model SA3100®, Coulter Co. Ltd, USA) was used to determine the BET specific surface area of clays under N_2 adsorption isotherms at 77 K.

2.5. Electrical conductivity measurements

Bulk electrical conductivity was measured in the thickness direction of isotropic molded films. The film with 20×20 mm^2 dimension was cut from four locations away from the edges and it was fixed on a glass slide using polyimide tapes. Silver paste was used to ensure good contact between the film surface and the copper electrodes. The film attached glass slide was placed in a chamber and the bulk conductivity was measured at room temperature by using a Keithley 6487 picoammeter® equipped with a direct current voltage source. The applied voltage was controlled within the range (0.001–500 V). The bulk electrical conductivity of the isotropic films was determined from average conductivities of four different locations on the compression-molded part and each set of measurement were repeated three times for all compositions.

2.6. Rheological measurements

An Advanced Rheometric Expansion System (ARES Rheometrics®, TA Instruments, USA) with a parallel-plate fixture (25 mm diameter) was used to execute dynamic frequency sweep experiments by using compression-molded disks in frequency range (0.1–100 rad/s) under nitrogen blanket. A fixed strain of 10% was used and the frequency sweep experiment at 230, 240, and 250 °C within ±1 °C fluctuation lasted for about 480 s. Dynamic time sweep experiments under isothermal conditions were executed at $\omega=0.1$ rad/s for about 1000 s. By using the same mode, we captured sheared samples for nylon 6/CB ($\phi=0.109$) system with 5 vol% organoclay-loading and organoclay/nylon 6 (0.05/0.95) system at $\omega=50.0$ rad/s, respectively, following by rapid cooling for subsequent TEM study to investigate the state of orientation in clay and carbon black particles.

2.7. Scanning electron microscopy (SEM)

The state of CB dispersion was observed by means of a field emission type SEM (Model JSM5310®, JEOL, Japan) on isotropic molded films by freeze-fractured in liquid nitrogen. The fracture surface was coated by the Polaron high energy silver sputtered device under vacuum atmosphere for 1 min before being observed in SEM.

2.8. Transmission electron microscopy (TEM)

All TEM images were taken at room temperature by a Philips TEM (Model FEI-TECNAI 12®) operated at 120 kV. Selected-area high-resolution observations (×135,000 magnification) were recorded with scanning Gaussian focus with bright-field image mode.

2.9. Electric force microscopy (EFM)

A Nano Scope IIIa with Multimode Scanning Probe Microscope Controller® and Phase Extender Box® (Digital Instruments/Veeco Metrology Group, USA) operated at bias voltage of 10 V and lift height of 40 nm with tapping mode were used for EFM imaging at room temperature. Single-crystal silicon probes coated with conductive platinum/iridium (Model SCM-PIT®, Veeco Probes, USA) with a spring constant 2.8 N/m were applied in this study. An electric field cantilever holder (Model MMEFCH®, Digital Instruments/-Veeco Metrology Group, USA) was employed for EFM imaging. Silver paste was used to ensure good contact between the sample and the metal substrates. Flat surfaces of bulk compression-molded part were used for the observation.

2.10. X-ray diffraction (XRD)

A horizontal wide angle X-ray diffractometer with Rigaku X-ray generator (Model RU-200B®) operated at 40 kV and 150 mA was used to obtain the diffraction profiles in (1.5–10.0°) 2θ range. The X-ray beam was monochromatized to

Cu Kα with detector arm mounted graphite crystal. Additionally, Bruker AXS® Generator equipped with a copper target tube and a two-dimensional detector was used to obtain the XRD patterns of isotropic molded films. The generator was operated at 40 kV and 40 mA. The X-ray beam was monochromatized to Cu Kα and the accumulation time of 20 min was used.

3. Results and discussion

3.1. Electrical percolation behavior

Electrical percolation behavior for nylon 6 loaded with a series of CB concentrations is shown Fig. 2. Percolation threshold (V_f^*) is defined as the critical CB volume fraction (ϕ) where the conducting network is formed. The formation of conducting network does not require direct contact between adjacent CB aggregates. They just need to be close enough on the order of nanometers for electron tunneling (or electron hopping) over the potential barriers at the gaps [17]. In the absence of organoclay, the increase of CB to $\phi=0.155$ enhances the electrical conductivity of nylon 6/CB system by three orders of magnitude as shown in Fig. 2(a). The electrical percolation behavior of this binary system has much higher V_f^* with shallower slope of percolation curve as compared to polyolefin/CB mixtures [19]. This is due to the contribution of polar component to surface tension that decreases the interfacial tension and enhances bonding to CB. This results in the reduction in CB mobility leading to delay in long-range network formation. A most striking feature of Fig. 2(a) is the significant decrease in V_f^* to $\phi=0.058$ when organoclay volume fraction was increased to 3 vol%. The V_f^* increases to $\phi=0.109$ as we further increase the organoclay-loading to 5 vol% and it is located between 0 and 3 vol% organoclay-loaded nylon 6/CB systems. This suggests that there is an optimum organoclay volume fraction to enhance electrical conductivity. We also observe three novel percolation features: (i) with the decrease of organoclay-loading, the slope of percolation curves decreases to 3 (5 vol% loading), 2.5 (3 vol% loading), and 1.5 (0 vol% loading) in the percolating regions, respectively, (ii) the electrical conductivity shows a higher value at higher CB volume fraction region in the $\phi=0.155$–0.197 range as organoclay-loading increases, and (iii) accordingly, the effective concentration of organoclay can be optimized to control the level of the percolation curve such as 3 vol% organoclay-loading with a consistent electrical conductivity in the 10^{-6}–10^{-7} S/cm range.

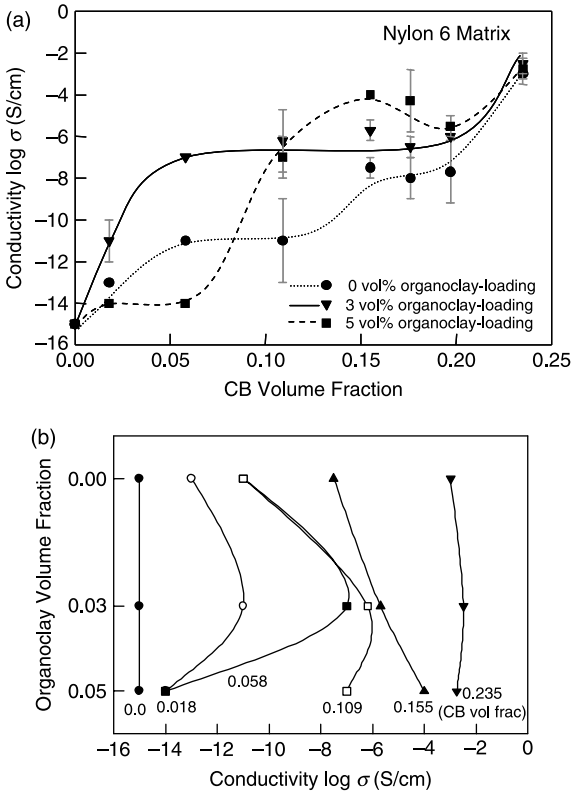

Fig. 2. (a) Plots of log σ versus CB volume fraction at room temperature for various nylon 6/CB systems: (●) 0 vol% organoclay-loading, (▼) 3 vol% organoclay-loading, and (■) 5 vol% organoclay-loading. (b) Cakmak–Konishi plot of organoclay volume fraction versus log σ at various CB volume fractions.

Fig. 2(b) shows an overview of organoclay-loading induced percolation phenomenon in nylon 6/CB systems. The electrical conductivity data at 3 vol% organoclay-loading indicates that CB network forms in the first stage. In the second stage, the electrical conductivity data of 5 vol% organoclay-loading begins to take off. This is a delay of percolation and the electrical conductivity data crosses over the 3 vol% organoclay-loading. In the final stage, the electrical conductivity data for all nylon 6/CB systems become nearly linear regardless of organoclay-loading level. This novel electrical percolation behavior shown in Fig. 2 does not fit into any known categories of conventional electrical percolation behavior in the published literature [1,2,4–14,19–23,25–40]. It should be noted that, in this study, we chose to use low-structure rubber grade CB and it exhibits compact primary aggregates comprised of fewer primary particles making it difficult to disperse and develop percolating network structure by self-agglomeration within the nylon 6 matrix.

3.2. Dispersion and distribution of carbon and clay nanoparticles

Fig. 3(a)–(c) show scanning electron microscopy (SEM) images of nylon 6/CB ($\phi=0.058$) systems with various organoclay-loading, where the white (or black) spots (depending on positive or negative image) represent the primary CB aggregate and the dark (or gray) areas represent the nylon 6 matrix. The left half of each image is the original and the right half is the digitally enhanced image of one contiguous SEM image to show that digital enhancements do not change the bulk information in these images. Fig. 3(d) schematic helps one to interpret the SEM images. With the increase of organoclay concentration from 0 to 3 vol%, one can observe the changes in CB dispersion in Fig. 3(a) and (b). Upon increase of organoclay, the dispersion metastasizes into 'branching' and/or 'chaining' morphology. This observation is in accord with the fact that

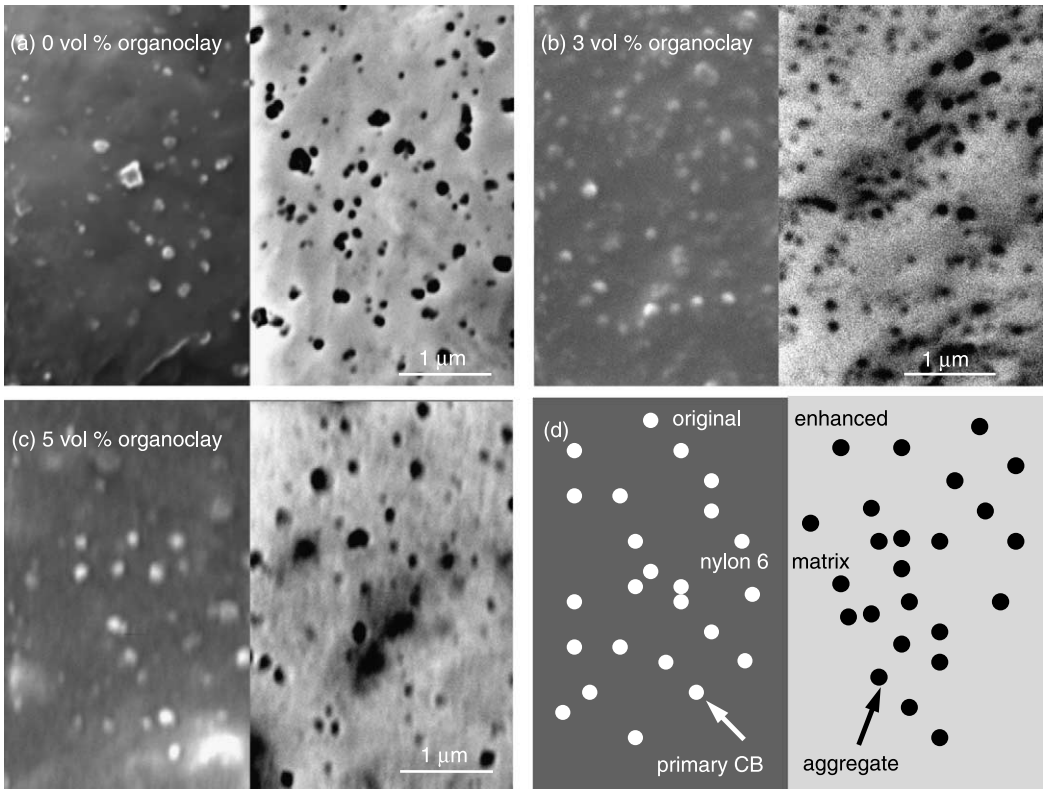

Fig. 3. SEM images of various nylon 6/CB ($\phi = 0.058$) systems: (a) 0 vol% organoclay-loading, (b) 3 vol% organoclay-loading, and (c) 5 vol% organoclay-loading, where the white (or black) spots represent the primary CB aggregate and the dark (or gray) areas represent the nylon 6 matrix. Left is the original and right is the enhanced of divided single SEM image. (d) Schematic of interpretation of the SEM images.

nylon 6/CB system with 3 vol% organoclay-loading achieves percolation at $\phi = 0.058$, where it is at the V_f^* as shown in Fig. 2(a). We also observe that the state of CB dispersion does not show percolating structure as the organoclay-loading increases to 5 vol% since $\phi = 0.058$ is not at the V_f^* for nylon 6/CB system with 5 vol% organoclay-loading.

In support of the above statement, Fig. 4(a) and (b) show SEM images of nylon 6/CB ($\phi = 0.109$) system. A well-developed 'fish-net' morphology with co-continuous CB network structure is observed in Fig. 4(b), where $\phi = 0.109$ is the V_f^* for nylon 6/CB system with 5 vol% organoclay-loading. In the absence of organoclay (Fig. 4(a)), scattered CB aggregate morphology is observed from the system that has not reached V_f^*. This novel structural development and electrical property variation in Figs. 2–4(b) clearly related to the presence of organoclay in the mixture leading to a novel percolation phenomenon.

To further clarify and quantify the morphological features in Figs. 3 and 4, we conducted image analysis on all SEM photographs. Fig. 5 shows the histogram of the distribution of nearest neighbor lengths on carbon aggregates for nylon 6/CB ($\phi = 0.058$) systems and nylon 6/CB ($\phi = 0.109$) systems with various organoclay-loading. Referring to Fig. 5, sharp peaks of histogram appear at 200 nm, where it is located at the shorter

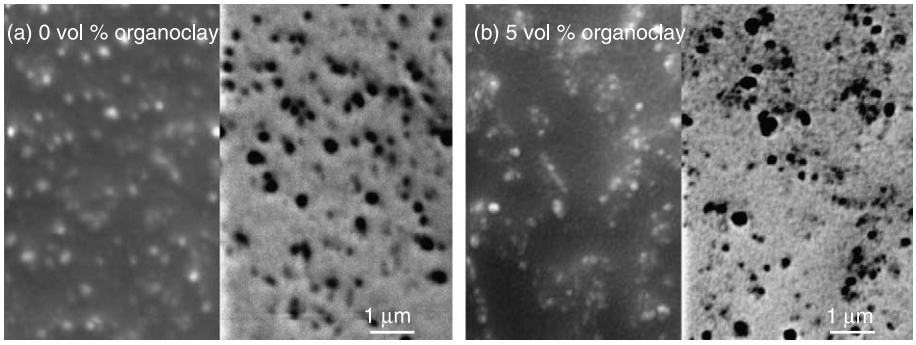

Fig. 4. SEM images of various nylon 6/CB ($\phi = 0.109$) systems: (a) 0 vol% organoclay-loading and (b) 5 vol% organoclay-loading, where the white (or black) spots represent the primary CB aggregate and the dark (or gray) areas represent the nylon 6 matrix. Left is the original and right is the enhanced of divided single SEM image.

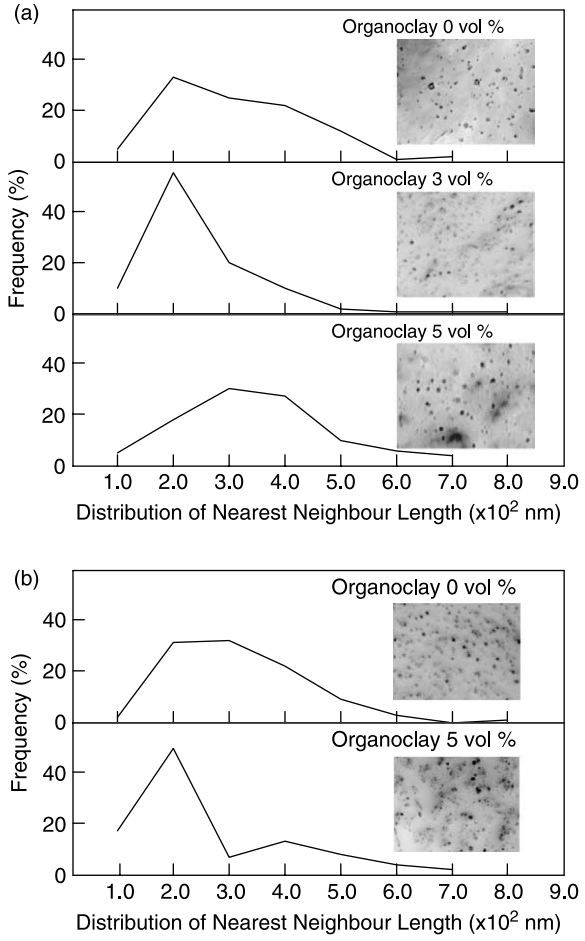

Fig. 5. Histogram of the distribution of nearest neighbour length for: (a) nylon 6/CB ($\phi = 0.058$) systems and (b) nylon 6/CB ($\phi = 0.109$) systems with various organoclay-loading. The inset gives the SEM images of each system, respectively, for subsequent image analysis (all images are enhanced).

distance side in the histogram for 3 vol% (Fig. 5(a)) and 5 vol% (Fig. 5(b)) organoclay-loadings, respectively. The data indicate that the nearest neighbor distance is less than 200 nm for CB aggregates to construct percolating network structure in nylon 6 matrix. This observation is worth nothing to support Fig. 2 because $\phi = 0.058$ and 0.109 are at the V_f^* for nylon 6/CB systems with 3 and 5 vol% organoclay-loadings, respectively.

Quantitative image analysis on the state of CB dispersion is characterized by utilizing the quadrate method of Morishita and Morishita's I_δ index [26,46–50]. First proposed by ecologists [46] to analyze the distribution of antlions' nests in a sand box, in this method, a total area of an image is divided into elementary parts of equal area. The number of points in each element is then determined. Each CB aggregate is regarded as one dot in this study as shown in the inset of enhanced SEM images in Fig. 5. The variation of CB dispersion pattern against Morishita's I_δ index as a function of quadrate number q, which is expressed by

$$I_\delta = q\delta \tag{1}$$

with

$$\delta = \frac{\sum_{i=1}^{q} n_i(n_i - 1)}{N(N-1)} \tag{2}$$

where q is the number of elemental parts equally divided from the total area of the SEM images, n_i is the number of primary CB aggregate regarded as one dot in the ith section of the SEM images, and N is the total number of primary CB aggregates regarded as dots.

$$N = \sum_{i=1}^{q} n_i \tag{3}$$

Image analysis for this study is conducted [48] based on the Eqs. (1)–(3). Fig. 6 schematic helps in the interpretation of the relationship between Morishita's I_δ index and q for various distribution modes of primary CB aggregates according to the theory. Fig. 7 shows the the SEM images

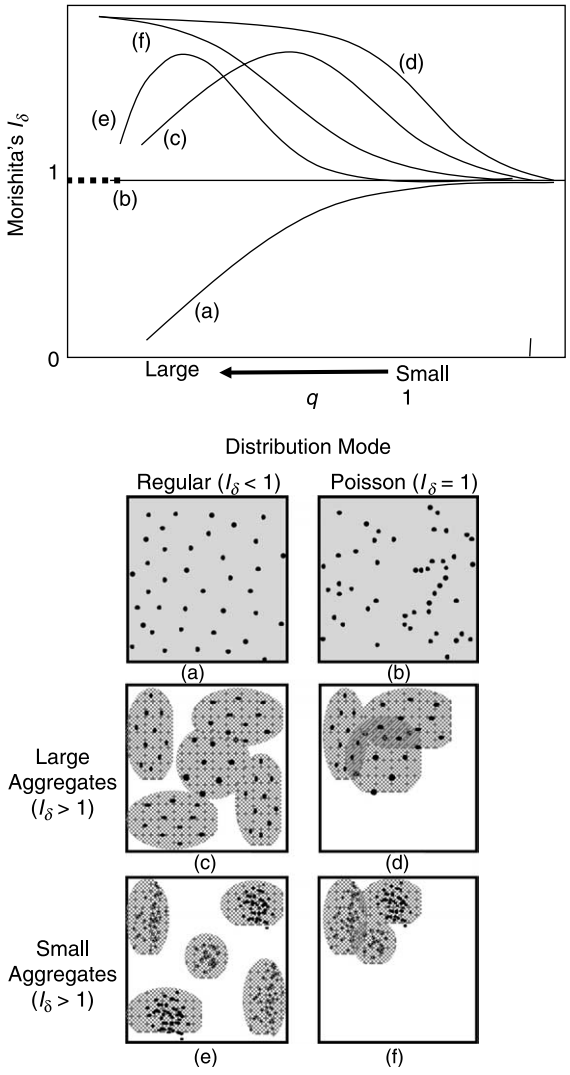

Fig. 6. Schematic of the relation between Morishita's I_δ index and dividing number q for various distribution modes of primary CB aggregates.

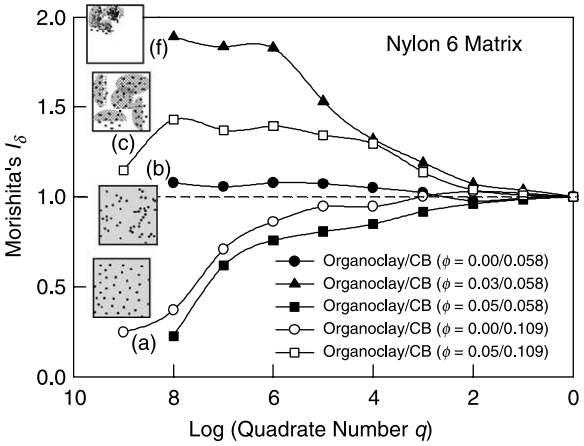

Fig. 7. Plots of Morishita's I_δ index versus dividing number q for various nylon 6/CB systems with various organoclay-loading. The inset with symbol gives the corresponding schematic and curve in Fig. 6 for various distribution modes of primary CB aggregates.

and Morishita's I_δ index versus dividing number q for nylon 6/CB ($\phi = 0.058$ and 0.109) loaded with a series of clay concentrations. The following are some of the salient features of data presented in Figs. 2–5: (i) with the increase of organoclay-loading for nylon 6/CB ($\phi = 0.058$) systems, the Morishita's I_δ indices vary in order of $I_\delta = 1$ (0 vol% loading), $I_\delta > 1$ (3 vol% loading), and $I_\delta < 1$ (5 vol% loading). These values correspond to distribution modes indicated by symbols (b), (f), and (a) shown in Fig. 6, respectively. The above observation indicate that at 0 vol% organoclay-loading CB aggregates exhibit scattered morphology following Poisson distribution. With the increase of organoclay-loading to 3 vol%, the distribution changes to aggregated mode with small size aggregates distributed within Poisson mode as a whole. At the final stage of organoclay-loading, the distribution becomes regular. (ii) For nylon 6/CB ($\phi = 0.109$) systems the Morishita's I_δ indexes are: $I_\delta < 1$ for 0 vol% organoclay-loading and $I_\delta > 1$ for 5 vol% organoclay-loading. These values correspond to (a) and (c) distribution modes shown in Fig. 6, respectively. The presence of organoclay alters the distribution of CB aggregates from regular mode to aggregated mode with large size aggregates distributed within regular mode as a whole. Thus, CB dispersion in the nylon 6 matrix is forced to form percolating network structure by the presence of organoclay at low to intermediate optimum organoclay-loading levels.

In order to examine the morphological hierarchy developed in organoclay/nylon 6/CB ternary nano system, we used X-ray diffraction (XRD) and transmission electron microscopy (TEM) techniques. Fig. 8(a)–(c) show XRD patterns for nylon 6 systems with various organoclay-loading and corresponding TEM bright-field images on selected samples. In TEM images, the dark layers represent organoclay platelets typically oriented edge-on and gray/white areas represent the nylon 6 matrix. The XRD patterns for nylon 6 nanocomposites do not show any discernible diffraction peak and they indicate full exfoliation in these systems. These results are also confirmed by the TEM images.

Fig. 8(d) and (e) show XRD patterns for nylon 6/CB ($\phi = 0.058$) systems with varying organoclay-loading. Although it is filled with significant amount of CB in the nylon 6 nanocomposites, XRD profiles indicate 'a fully exfoliated clay structure'.

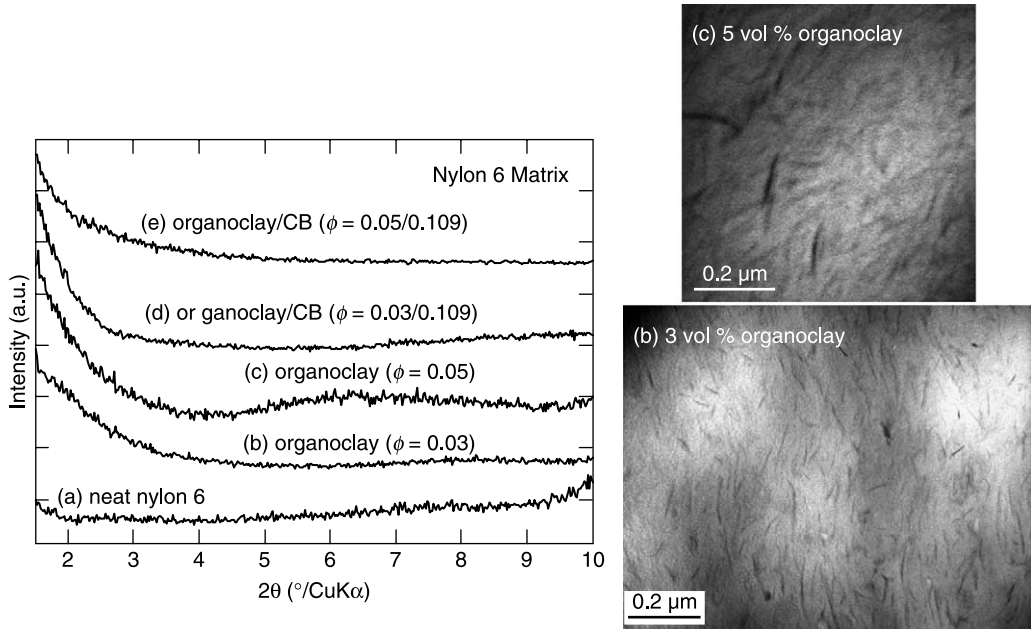

Fig. 8. XRD patterns for various nylon 6 systems: (a) 0 vol% organoclay-loading, (b) 3 vol% organoclay-loading, and (c) 5 vol% organoclay-loading with TEM images, where the dark layers represent the organoclay platelets and the gray/white areas represent the nylon 6 matrix (all images are enhanced) and XRD patterns for various nylon 6/CB ($\phi = 0.109$) systems: (d) 3 vol% organoclay-loading and (e) 5 vol% organoclay-loading.

3.3. Morphology of carbon and clay nanoparticles dispersed in polymer: isotropic systems

TEM images of isotropic nylon 6/CB ($\phi = 0.109$) systems with varying organoclay-loading are shown in Fig. 9(a) and (b). In these images, the dark spherical areas represent the primary CB aggregate and the gray/white areas represent the nylon 6 matrix. The arrow indicates the organoclay platelet (or the dark single layer). We observe two distinct morphological features: (i) CB/organoclay behave as if one 'nano-unit' structure in nylon 6 matrix regardless organoclay loading levels. The presence of this 'nano-unit' morphology suggests that there are strong preferred intermolecular interactions between organoclay/nylon 6/CB. (ii) A striking feature in Fig. 9 is that the organoclay platelets essentially deform to wrap partially around the rigid primary CB aggregates following its contours. The observed morphology indicates that the organoclay platelets roughly 5.0 nm in thickness has a certain flexibility and they are bent around the 60.0 nm diameter CB particles without fracture. They, however, do not touch CB particles. The distance between CB particles and adjacent organoclay platelets are on the order of 5.0–20.0 nm range that correspond to the presence of different amounts of nylon 6 and organic modifier between these particles.

Since, the development of the first atomic force microscopy (AFM) by IBM group [49] in 1986 wide range of variants of this technique has found utility throughout the scientific community [51]. One particular version is sensitive to the spatial variations of electrical fields and local conductivities [51,52] called electric force microscopy (EFM). In this technique spatial variations of electrostatic force can be detected by its influence on frequency of vibrating conductive probe hovering above the sample being investigated. This allows rapid determination of the local variations of electrical conductivity as electrical fields differ between conductive and non-conductive regions. In this technique, a first scan is performed along a line in the tapping mode (motion 1). This provides the topography of surfaces. Following the first scan, the probe lifts to a predetermined height (motion 2) and a second scan (motion 3) immediately executes along the same path as the motion 1. These motions alter the probe resonant frequency and its phase in accord with the contours of the surface and the strength of the local electrical field dictated by the local variation of electrical conductivity. The results are mapped with the phase image representing conducting regions as dark and insulating regions as bright. Yerina et al. [51] and Viswanathan et al. [52] applied EFM to direct visualization the percolating network structure in polymer matrices.

In order to augment the 'nano-unit' morphology observed by high-resolution TEM in cross-sectional view we performed EFM of the same are on the surface. Fig. 10 shows high-resolution EFM phase surface image of the sample obtained from isotropic nylon 6/CB ($\phi = 0.109$) system with 5 vol% organoclay-loading. In these images, the dark areas represent

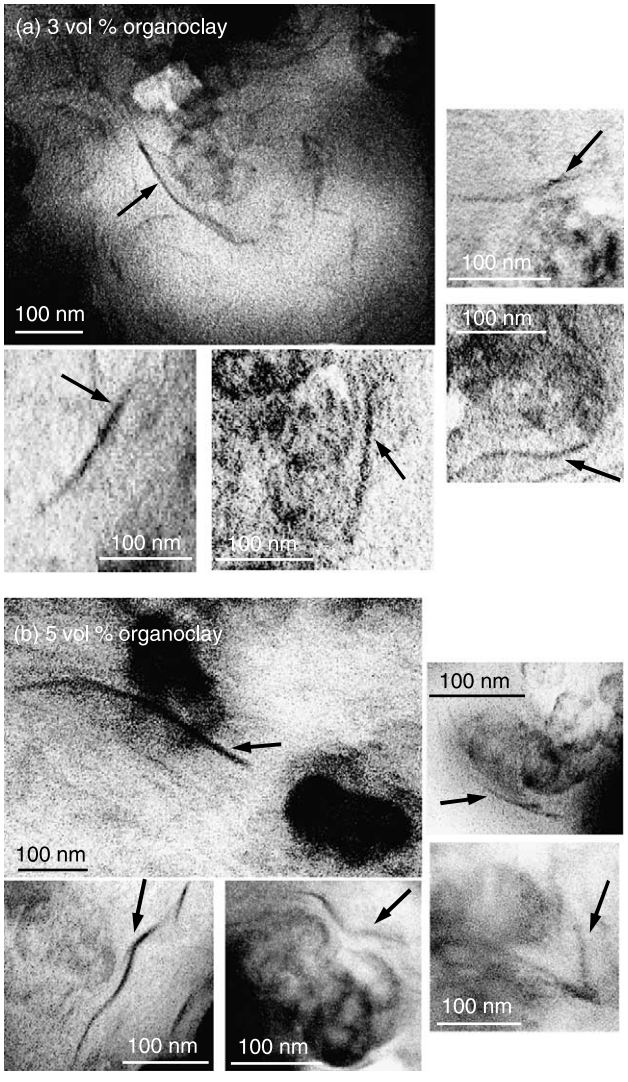

Fig. 9. TEM images of various nylon 6/CB ($\phi = 0.109$) systems: (a) 3 vol% organoclay-loading and (b) 5 vol% organoclay-loading, where the dark spherical areas represent the primary CB aggregate and the gray/white areas represent the nylon 6 matrix. The arrow or the dark layer indicates the stacked organoclay platelets (all images are enhanced).

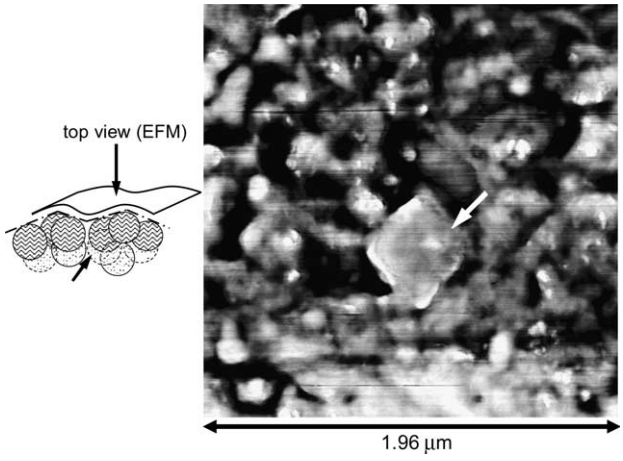

Fig. 10. EFM phase image of nylon 6/CB ($\phi = 0.109$) system with 5 vol% organoclay-loading, where the dark areas represent the CB-enriched conducting regions and the gray/white areas represent the nylon 6 matrix and/or organoclay insulating regions. The arrow indicates the single organoclay platelet (original image).

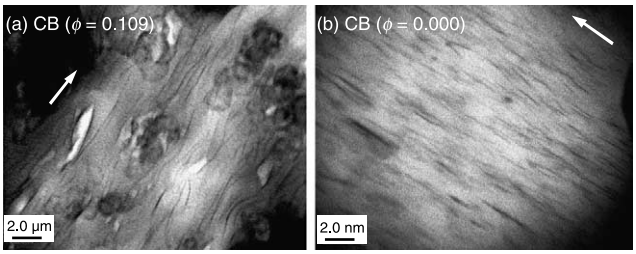

Fig. 11. TEM images of various extruded nylon 6 systems: (a) nylon 6/CB (ϕ = 0.109) system with 5 vol% organoclay-loading (screw speed 200 rpm at 230 °C) and (b) organoclay/nylon 6 (0.05/0.95) system, where the dark spherical areas represent the primary CB aggregate, the dark layers represent the organoclay platelets, and the gray/white areas represent the nylon 6 matrix. The shearing direction is indicated by the arrow (all images are enhanced).

the CB-enriched conducting regions and the gray/white areas represent the nylon 6 matrix and/or organoclay insulating regions. The arrow points to a single organoclay platelet viewed face-on on the surface. We clearly observe the platelet geometry of organoclay as well as the 'nano-unit' structure from top view as expected. It suggests that CB aggregates located under the wide surface area of organoclay platelet without fracture. The combination of high-resolution TEM and EFM revealed three-dimensional organoclay/CB 'nano-unit' morphology.

3.4. Morphology of carbon and clay nanoparticles dispersed in polymer: influence of shearing

To investigate the effect of thermo-mechanical history on 'nano-unit' morphology of organoclay/CB behavior we examined the as extruded samples that went through shearing during compounding as well as compression-molded disks of various nylon 6 systems subjected to isothermal shearing by using rheometry. Fig. 11(a) and (b) show TEM images of extruded parts and Fig. 12(a)–(c) show TEM images of sheared parts, where the dark spherical areas represent the primary CB

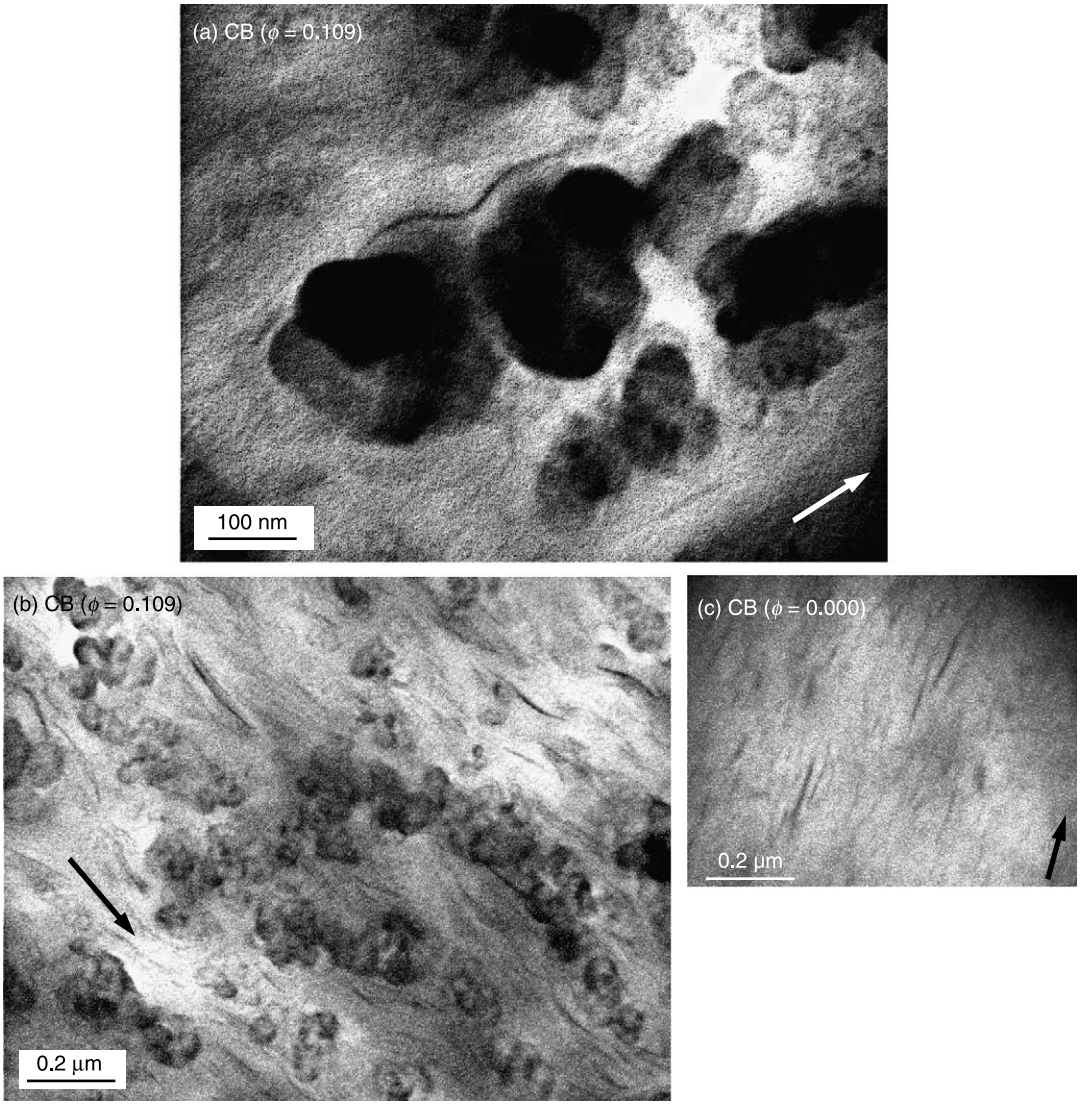

Fig. 12. TEM images of various sheared nylon 6 systems (ω = 50 rad/s at 230 °C for 200 s): (a) and (b) nylon 6/CB (ϕ = 0.109) system with 5 vol% organoclay-loading and (c) organoclay/nylon 6 (0.05/0.95) system, where the dark spherical areas represent the primary CB aggregate, the dark layers represent the organoclay platelets, and the gray/white areas represent the nylon 6 matrix. The shearing direction is indicated by the arrow (all images are enhanced).

aggregate, the dark layers represent the organoclay platelets, and the gray/white areas represent the nylon 6 matrix. The shearing direction is indicated by an arrow. The organoclay dispersion in both extruded and sheared organoclay/nylon 6 (0.05/0.95) systems (Figs. 11(b) and 12(c)) clearly shows that organoclay platelets become stacked and oriented with their broad surfaces in the shearing plane as expected. This entrainment phenomenon was also observed by a glass spheres during shear flow in suspensions [53]. The presence of irregular shaped CB cluster and network induces local redirection of these stacked organoclay platelets but they preserve local parallelism with each other (Figs. 11(a) and 12(b)). Fig. 12(a) clearly shows the 'nano-unit' of CB aggregates and organoclay platelets intimately following its local contours without fracture even in the shearing fields. This provides further evidence on the strength of interfacial bonding between organoclay/nylon 6/CB via preferred intermolecular interactions with novel features on the flexibility of clay nanoplatelet.

3.5. Nature of clay bending in self-assembly organoclay/CB 'nano-unit' structure

In this work, we observed bending of clay around CB particles forming 'nano-unit' morphology throughout the percolating network. No reports on the rigidity of the clay platelet dispersed in polymer melts are available in the literature at present. Very few studies [54–59] addressed the rigidity and curvature mechanism of clay minerals mainly by mineralogists [54]. The first known literature on clay curvature mechanism is attributed to Pauling [55] in 1930. He recognized that the bending tendency for layered silicates is not only caused by external mechanical forces but also by the relief of internal stresses generated by the mismatch of magnesium octahedral and silicon tetrahedral sheets in 1:1 type layers. The layered silicates commonly known as clay minerals in nature considered 'brittle' material especially the ones called a dioctahedral 2:1 type layers the smectite group of minerals with a specific term 'montmorillonite' commonly used for polymer–clay nanocomposites. The large surface area offers a high cation exchange capacity within the layers and tends to orient polar molecules offering adsorption/intercalation opportunity for various organic compounds. Extensive XRD [54] and TEM [56] studies identify the brittle structure of montmorillonite and it shows a single layer of aluminum octahedral sheet sandwiched with two layers of silicon tetrahedral sheets in highly packed well-developed crystalline layer but it has variable basal spacings with turbostratic stacking of the layers. Montmorillonite exhibits monoclinic unit cell with $a=5.17$ Å, $b=8.94$ Å, $c=9.95$ Å, $\alpha=\gamma=90°$ and $\beta=100°$. The inherent mismatches between the octahedral and double tetrahedral sheets induce hexagonal symmetry leading curvature of the layers caused by the process of relieving internal stresses. Solin et al. [57] proposed a discrete model and predicted the rigidity of a host clay layer in binary intercalation compound and found correlation between the rigidity of a host layer and composition-dependent basal spacing of inter-silicate layers. Oya et al. [58] emphasized the relation between clay morphology and mechanical properties of polypropylene (PP) nanocomposites. They stated that clay morphology with stiff well-developed crystalline layers (montmorillonite and mica) induces higher reinforcement effects then flexible loosely stacked layers (hectorite) in PP nanocomposites. Yalcin et al. [59] first presented morphological evidence on the fracture behavior of primary organoclay platelet in poly(vinyl chloride) nanocomposites by AFM. They revealed that primary organo-montmorillonite platelets dispersed in polymer are brittle and fractured during dispersion.

Morphological evidence of organoclay/CB 'nano-unit' on TEM images (Figs. 9–12) presented in this study indicates that these clay platelets are rather flexible within a tolerance range of curvature. Based on these measurements, the radius of curvature ranges from 7.4 to 20.0 nm with the mean value of 15.1 nm for organo-montmorillonite platelets dispersed in polymer melts. These are larger than the reported values 4.0–14.0 nm for the curvature range [60,61] and 8.8 nm for the mean curvature value [60,61] of the pristine natural chrysotile tubes directly observed by Yada [60,61]. We also realized that the centre part of the platelets are thicker than the edges of the organoclay platelets (Fig. 9). The centre thickness of the bent clay is about 7.0 nm (note that the thickness increases 2.0 nm from the original unbend organoclay platelets) and the edges thickness are roughly 2.0 nm (note that the thickness decreases 0 nm from the original unbend organoclay platelets). These observations suggest that the organoclay curvature observed in 'nano-unit' structure is originated from 4 to 5 stacks of a primary organo-montmorillonite platelet in a leaf spring appearance with tapered ends. This morphology allows the stacked layers to be bent in the polymer melts.

We now offer an explanation on the morphologically observed bending nature of stacked organo-montmorillonite platelets curvature under the presence of CB dispersed in polymer melts. The morphological evidence on the fracture behavior presented by Yalcin et al. [59] explains the limitation of primary organo-montmorillonite platelet curvature dispersed in polymer melts under shear mixing in the absence of CB. Although no reports on the effect of chemical modification on the clay curvature dispersed in polymer melts are available at present, we attribute the bending nature of stacked organoclay platelet curvature to a combination of strong attraction of local intermolecular forces induced by organoclay/nylon 6/CB interactions and local internal pressure originated from instability of shearing fields. Our hypothesis is that the strong attraction of intermolecular forces between polymer chains and pristine clay surfaces with selected organic modifier enhances the range of the clay platelet curvature.

3.6. Influence of nanoparticles on the nylon 6 phase behavior

Nylon 6 exhibits stable α form [62] by crystallization from the melt by slow cooling exhibiting characteristic (202 + 002 mixture), (200) crystalline planes belonging to monoclinic [62] unit cell with $a=9.56$ Å, $b=17.24$ Å (chain axis), $c=8.01$ Å, and $\beta=67.5°$. The γ form [63] can be obtained by quenching

from the melt exhibiting characteristic (001), (200), and (20$\bar{1}$) diffraction planes also of monoclinic form with reported values [64] of $a=9.33$ Å, $b=16.88$ Å (chain axis), $c=4.78$ Å, and $\beta=121.0°$.

Fig. 13(a)–(c) show XRD patterns for nylon 6/CB/NC ternary systems. The crystal structure of neat nylon 6 shows a mixture of α and γ forms with two intense α diffraction peaks (plane 200 and 202+002 doublet) and single intense γ diffraction peak (plane 001, 200, and 20$\bar{1}$) as shown in Fig. 13(a). In the presence of CB, the γ diffraction peak disappears and two α diffraction peaks are enhanced despite the low CB volume fraction ($\phi=0.018$). As we further increase the CB volume fraction to $\phi=0.235$, the crystal structure of nylon 6 still remains in α form and this is also observed in the presence of silicate layers (Fig. 13(b) and (c)). The above observations indicate that addition of CB to nylon 6 favors the α crystalline structure formation in nylon 6 phase structure. We attribute this mainly to nucleating effects of both CB and clay nanoplatelet that cause the crystallization of nylon 6 to take place at higher temperatures where the α crystal formation is favored.

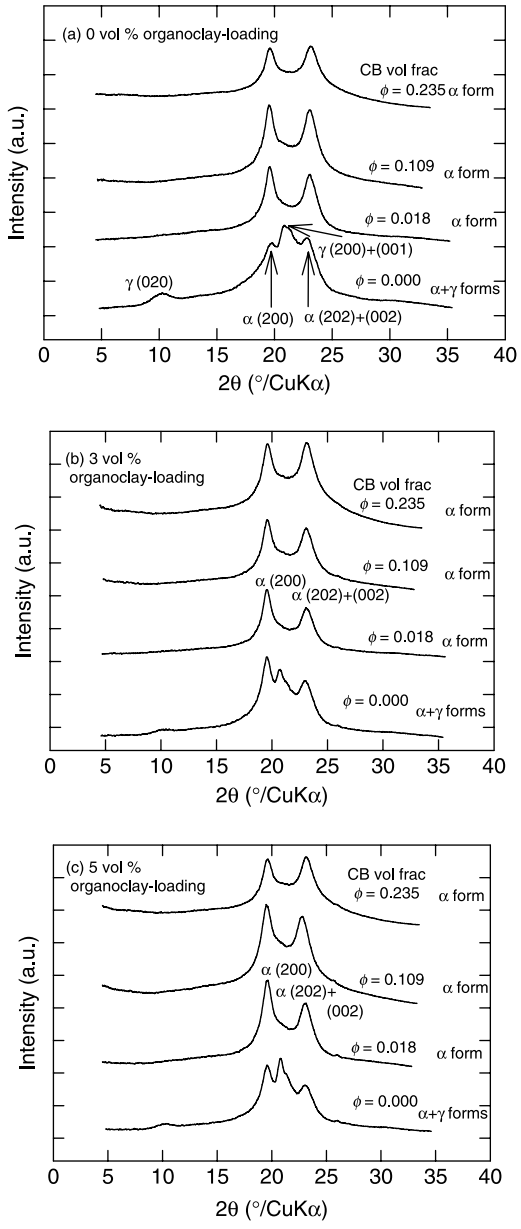

Fig. 13. XRD patterns for various nylon 6/CB systems: (a) 0 vol% organoclay-loading, (b) 3 vol% organoclay-loading, and (c) 5 vol% organoclay-loading at various CB volume fractions.

3.7. Linear dynamic viscoelastic properties

Early in the 1960s, Payne [64] found that CB aggregate structure affects the dynamic viscoelastic properties of rubber mixtures and specifically elastic modulus decreases with increasing strain amplitude (Payne effect). Payne's results [64] were quantified by Kraus [65] and following Nielsen et al. [68] emphasized that variations of dynamic viscoelastic properties for polymer–carbon composites are well correlated with the structural variations described by a modified Kerner equation [67]. There are extensive reports [68–72] on linear dynamic viscoelastic properties of polymer–carbon composites in connection with electrical percolation behavior.The polymer–carbon composites with CB volume fraction above V_f^* exhibit strong shear-thinning and/or yield behavior at very low ω of $|\eta^*|$ and G' in oscillatory shear flow at molten state due to the existence of percolating structure [72].

Fig. 14(a)–(c) show log G' versus log ω plots for nylon 6/CB/NC systems w at 250 °C. The values of G' in the lowest ω increase with increasing CB volume fraction in nylon 6/CB system (Fig. 14(a)). As the CB volume fraction further increased, the slope of log G' versus log ω plots in the terminal region for all nylon 6/CB systems becomes much less than 2. This suggests that the bulk structure in a fluid exhibits a behavior intermediate between solid-like and liquid-like states associated with the degree of CB network formation. The terminal region of log G' versus log ω plots has a pronounced 'yield behavior' in all CB filled systems. This indicates that G' is sensitive to the structural variations on the density and strength of percolating networks; thus, we focus on the behavior of G' in the terminal region.

Fig. 15 shows the G'_c/G'_p ratio of the storage modulus for nylon 6/CB system (G'_c) to the neat nylon 6 (G'_p) obtained from the the terminal region of Fig. 14. G'_c/G'_p values for nylon 6/CB systems with organoclay-loading exhibits higher values in the entire CB volume fraction range. This indicates the presence of organoclay results in enhancement in solid-like behavior.

Quantitative interpretation on the rheological features of G'_c/G'_p versus CB volume fraction plots is evaluated by applying the Nielsen model [66], which has been utilized for the quantitative estimation of percolating structure in polymer matrix with incorporating CB and other carbon nanoparticles [68,71].

$$\frac{G'_c}{G'_p}=\frac{1+AB\phi_f}{1-B\psi\phi_f}, \tag{4}$$

Here, G'_c/G'_p is the relative storage modulus at $\omega=0.1$ rad/s obtained from Fig. 15, ϕ_f is the volume fraction of CB, A is the

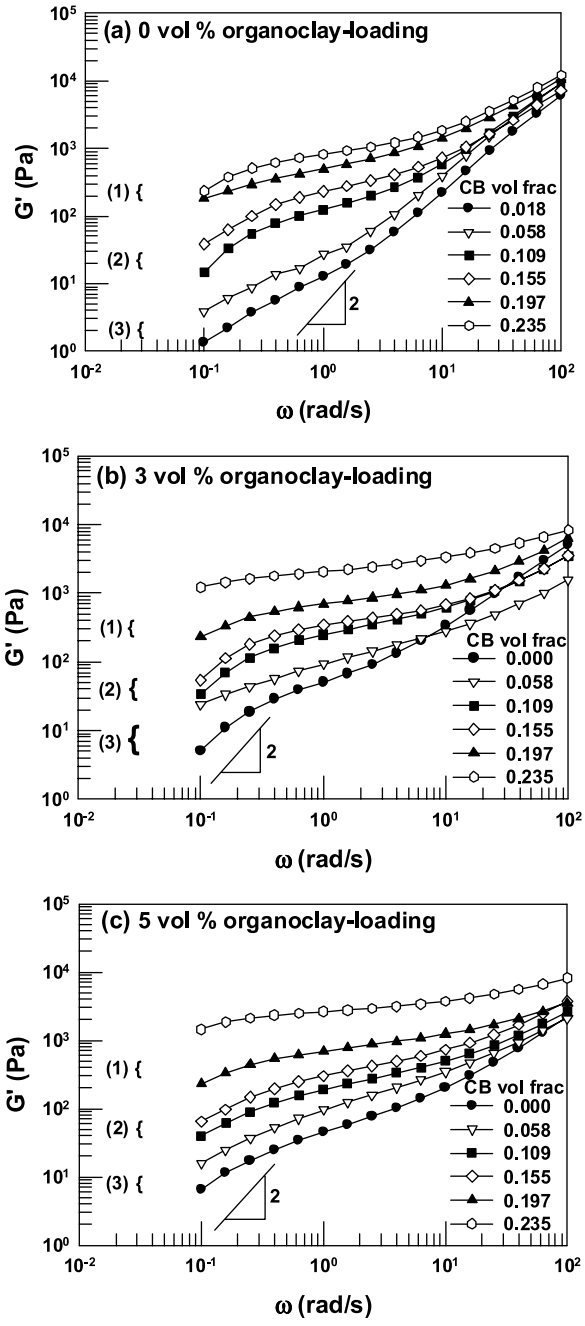

Fig. 14. Plots of log G' versus log ω at 250 °C for various nylon 6/CB systems: (a) 0 vol% organoclay-loading, (b) 3 vol% organoclay-loading, and (c) 5 vol% organoclay-loading with various CB volume fractions. (1) Limiting conducting region, (2) percolating region, and (3) insulating region.

CB flocculation index, which indicates the number of CB contacts per unit volume, B is the relative modulus of CB and polymer phases with the reported value 1.0 [66], and ψ is the factor that it depends on maximum packing fraction of CB with an empirical function and it fulfills the necessary boundary conditions defined as

$$\psi = 1 + \left(\frac{1-\phi_m}{\phi_m^2}\right)\phi_f \tag{5}$$

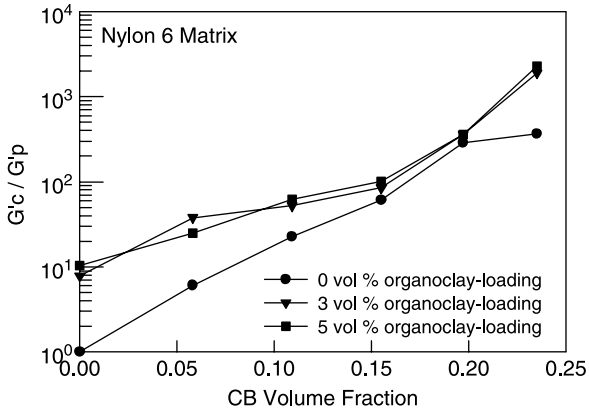

Fig. 15. Plots of G'_c/G'_p versus CB volume fraction at $\omega = 0.1$ rad/s and 250 °C for various nylon 6/CB systems: (●) 0 vol% organoclay-loading, (▼) 3 vol% organoclay-loading, and (■) 5 vol% organoclay-loading.

where ϕ_m is the known maximum packing fraction for typical spherical carbon nanoparticles with the reported value 0.64 [66]. All the experimental data and calculated results are listed in Table 2. Fig. 16 shows the plots of log A versus CB volume fraction associated with the plots of log σ versus CB volume fraction for nylon 6/CB systems with various organoclay-loading. The following observations are worth nothing in Fig. 16: (i) Log A of 3 vol% organoclay-loading exhibits largest value at $\phi = 0.058$ and then level off. The electrical conductivity increases at $\phi = 0.058$ (Fig. 16). This corresponds to the V_f^* of 3 vol% organoclay-loaded nylon 6/CB system. (ii) As we further increase the CB volume fraction to $\phi = 0.109$, the log A of 5 vol% organoclay-loading exhibits roughly the same value as 3 vol% organoclay-loading. This behavior also corresponds to the significant increase of electrical conductivity, where it is the V_f^* of 5 vol% organoclay-loaded nylon 6/CB system. (iii) Finally, at the CB volume fraction of $\phi = 0.155$, where it is the V_f^* of organoclay-unloaded nylon 6/CB system, the log A reaches at similar level of organoclay-loaded nylon 6/CB systems. This indicates the completion of conducting network formation on all three systems. We obtain an average log A value 2.6, where it is the critical flocculation index for CB to form percolating network structure throughout the nylon 6 matrix. It should be pointed out that we showed the significant influence of organoclay-loading on the state of dispersion of CB in Section 3.6. The above observation is in accord with the fact that the variations of linear dynamic viscoelastic properties especially G' at terminal region for polymer–carbon composites are directly correlated with the variations of CB dispersion and we demonstrated that organoclay-loading induced advanced percolation phenomenon is monitored by tracing the variations of bulk structure in a fluid.

To support above statement, we subjected the isotropic molded disks of various nylon 6/CB ($\phi = 0.058$) systems to isothermal annealing at various temperatures at $\omega = 0.1$ rad/s in order to examine the temporal variations in G'. To facilitate our discussion below, we investigate the mobility of nylon 6 chains

Table 2
Experimental data: storage moduli of various nylon 6 systems at $\omega = 0.1$ rad/s and 250 °C; G'_c, relative storage moduli; $(G'_c - G'_{nano})/G'_p$ (storage moduli of neat nylon 6; G'_p and nylon 6 nanocomposites; G'_{nano}), electrical conductivity; σ, and calculated CB flocculation index; log A

Matrices	CB volume fraction	G'_c (pa)	$(G'_c - G'_{nano})/G'_p$	σ (S/cm)	log A
Neat nylon 6	0.000	0.635	1.000	10^{-15}	0.00
	0.058	862	6.081	10^{-11}	1.91
	0.109	14.475	22.792	10^{-11}	2.24
	0.155	38.466	60.567	$10^{-7.5}$	2.5
	0.197	182.434	287.252	$10^{-7.7}$	05
	0.235	23640	367.879	10^{-3}	05
3 vol% Organoclay/ nylon 6	0.000	5.043	0.000	10^{-15}	0.00
	0.058	24.239	30.223	10^{-7}	2.67
	0.109	3439	44.708	$10^{-6.2}$	2.54
	0.155	54.331	77.602	$10^{-5.7}$	2.6
	0.197	229.328	35132	10^{-6}	13
	0.235	1217.400	1908.832	$10^{-2.5}$	76
5 vol% Organoclay/ nylon 6	0.000	6.602	0.000	10^{-15}	0.00
	0.058	15.895	14.631	10^{-14}	2.34
	0.109	39.732	51.163	10^{-7}	2.61
	0.155	64.420	91.033	10^{-4}	2.67
	0.197	230.846	35068	$10^{-5.5}$	13
	0.235	1449.330	2271.548	$10^{-2.8}$	84

of zero-shear viscous flow. Fig. 17 shows an Arrhenius plot in log $|\eta_0^*|$ versus thermodynamic temperature with the inset plot of log $|\eta_0^*|$ versus various annealing temperature at $\omega = 0.1$ rad/s. We observe that $|\eta_0^*|$ decreases with increasing the annealing temperature with constant linear relationship (Newtonian behavior). This indicates that the increase of annealing temperature accelerates the mobility of nylon 6 chains with an apparent activation energy (E_a) of 21 kJ/mol obtained from the definition [77] of $\log(1/\eta_0^*) = \log A - (E_a/RT)$, where E_a is the activation energy of zero-shear viscous flow, R is the gas constant, T is the thermodynamic temperature, and η_0^* is the zero-shear viscosity.

3.8. Effect of annealing

Fig. 18(a)–(c) show log G' versus log t plots at $\omega = 0.1$ rad/s at a series of annealing temperatures for nylon 6/CB ($\phi = 0.058$) containing organoclay. The inset shows log G' versus log t plots at $\omega = 0.1$ rad/s for nylon 6 systems with various organoclay-loading in order to eliminate the CB filling effect. A most striking feature of Fig. 18(a) is that G' increases when the a critical time is reached (indicated by the arrow) for 0 vol% organoclay-loading. However, G' decreases over the entire range of annealing time for neat nylon 6 (the inset of Fig. 18(a)) presumably as a result of degradation of molecular weight during the test. This is also expected in the nylon 6 matrix with the compositions containing organoclay and CB. However, Fig. 18(b) and (c) indicates that the increase of G' is significantly affected by the presence of organoclay even without the incorporation of CB as shown in the insets. For instance, Fig. 18(b) shows significant increase of G' at 250 °C and this is in accord with the fact that 250 °C was the processing temperature (compression-molded) for 3 vol% organoclay-loaded nylon 6/CB system to achieve percolation at $\phi = 0.058$. This observation complements Figs. 2, 7, and 16 that the advanced percolation phenomenon observed at 3 vol% organoclay volume fraction is due to the effective organoclay-loading induced CB network self-assembly in nylon 6 matrix.

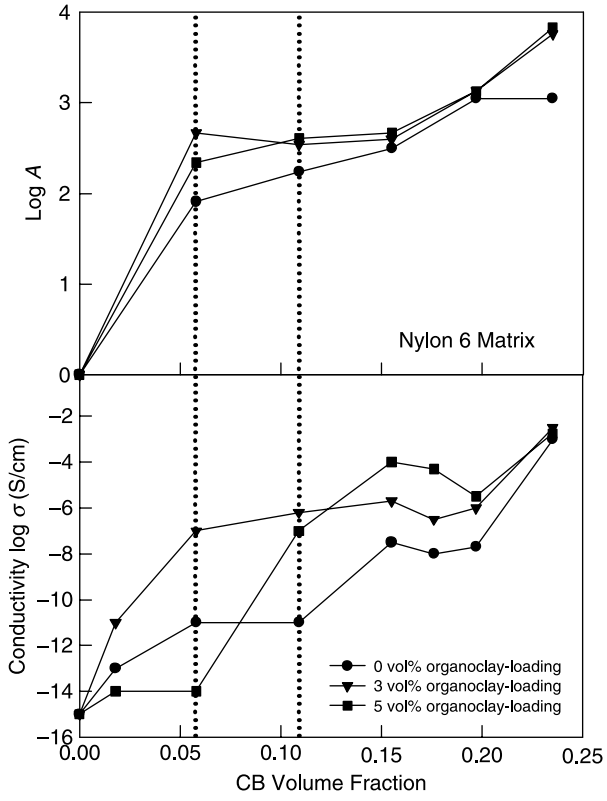

Fig. 16. Plots of log A versus CB volume fraction (upper figure) and plots of log σ versus CB volume fraction (lower figure) for various nylon 6/CB systems: (●) 0 vol% organoclay-loading, (▼) 3 vol% organoclay-loading, and (■) 5 vol% organoclay-loading.

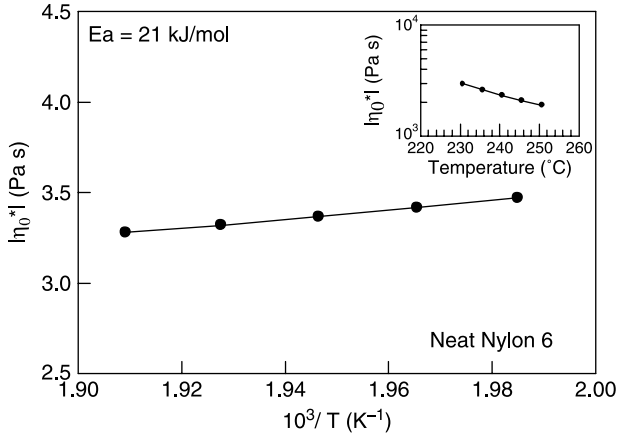

Fig. 17. Arrhenius plot in $\log|\eta_0^*|$ versus thermodynamic temperature with activation energy (E_a) of zero-shear viscous flow for neat nylon 6. The inset shows plot of $\log|\eta_0^*|$ versus temperature at $\omega=0.1$ rad/s for nylon 6.

The critical annealing time is defined as the rheological percolation time t_p. This has a parallel physical meaning with the electrical percolation time as defined by Wu et al. [31–33] With the increase of annealing temperature, the t_p shifts to a shorter annealing time in all nylon 6/CB ($\phi=0.058$) systems as illustrated in Fig. 18(a)–(c). This observation features similar characteristic of electrical dynamic percolation observed on polymer–CB composites in the literature. [31–33] Based on these results, Arrhenius analysis was performed to determine E_a of the rheological percolation time as shown in Fig. 18(d). In this figure, $\log t_p$ versus thermodynamic temperature plots for nylon 6/CB ($\phi=0.058$) systems with various organoclay-loading indicate a linear relationship. The calculated activation energies are 48, 65, and 70 kJ/mol for 0, 3, 5 vol% organoclay-loading, respectively. These activation energies of the rheological percolation time are directly correlated with the E_a—activation energy of flow as they both originated from the mobility of polymer chains. The data indicate that the nylon 6 chain mobility ($E_a=21$ kJ/mol) decreases in the presence of CB ($E_a=48$ kJ/mol) and the inclusion of organoclay ($E_a=65$–70 kJ/mol) further reduces the chain mobility due to the preferred intermolecular interactions between organoclay/nylon 6/CB. This observation is in accord with the morphological evidence of the organoclay/CB 'nano-unit' structure presented in previous Sections 3 and 4.

Table 3 and Fig. 19 show short summary of this work that we have discussed so far. The electrical percolation behavior exhibited remarkable shift in V_f^* with 3 vol% organo-montmorillonite volume fraction in nylon 6/CB system (see CB $\phi=0.058$ of Fig. 2(a)). The quantitative CB dispersion revealed that the distribution behavior altered very much in Poisson-aggregated-regular mode as the organoclay volume fraction changes in 0, 3, and 5 vol% order. The CB flocculation index obtained from rheological measurement complemented the above results: the number of CB contacts per unit volume in nylon 6/CB ($\phi=0.058$) system exhibits the largest value for

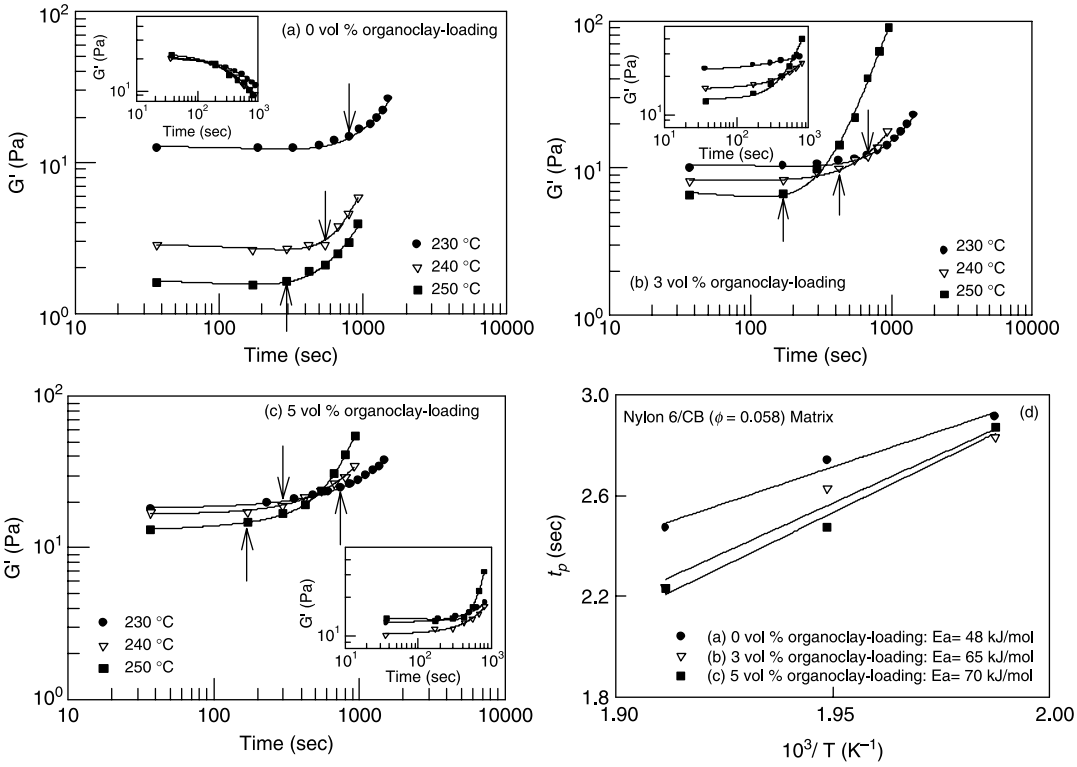

Fig. 18. Variations of $\log G'$ with $\log t$ during isothermal dynamic time sweep experiments at $\omega=0.1$ rad/s with various annealing temperatures for various nylon 6/CB ($\phi=0.058$) systems: (a) 0 vol% organoclay-loading, (b) 3 vol% organoclay-loading, and (c) 5 vol% organoclay-loading. The arrow indicates the rheological percolation time (t_p) and the inset shows plots of $\log G'$ versus $\log t$ at $\omega=0.1$ rad/s with various annealing temperatures for various nylon 6 systems: (a) 0 vol% organoclay-loading, (b) 3 vol% organoclay-loading, and (c) 5 vol% organoclay-loading. (d) Arrhenius plots in $\log t_p$ versus thermodynamic temperature with activation energy (E_a) of the rheological percolation time for various nylon 6/CB ($\phi=0.058$) systems.

Table 3
Percolation threshold (V_f^*), CB flocculation index (log A), rheological percolation time (t_p), activation energy (E_a), and Morishita's index (I_δ) for various nylon 6/CB ($\phi = 0.058$) systems

Nylon 6/CB systems	V_f^* (vol frac)[a]	log A[b]	t_p (s)[c]	E_a (kJ/mol)[d]	I_δ (mode)[e]
Neat nylon 6	–	–	–	21	–
0 vol% Organoclay	0.16	1.91	297	48	$I_\delta = 1$ (Poisson)
3 vol% Organoclay	0.06	2.67	170	65	$I_\delta > 1$ (aggregated)
5 vol% Organoclay	0.11	2.34	171	70	$I_\delta < 1$ (regular)

[a] Determined from Fig. 2(a).
[b] Determined from Table 2 for various nylon 6/CB ($\phi = 0.058$) systems.
[c] Determined from Fig. 19(a)–(c) at 250 °C for various nylon 6/CB ($\phi = 0.058$) systems.
[d] Determined from Figs. 18 and 19(d) for neat nylon 6 and various nylon 6/CB ($\phi = 0.058$) systems.
[e] Determined from Fig. 7 for various nylon 6/CB ($\phi = 0.058$) systems.

3 vol% organoclay volume fraction. This indicates the early completion of percolating network structure in all three systems. Fig. 19 shows plots of t_p versus organoclay volume fraction at various annealing temperatures (left axis) and plots of E_a versus organoclay volume fraction (right axis) for nylon 6/CB ($\phi = 0.058$) system. This figure indicates that advanced percolation phenomenon is temperature and organoclay-loading dependent. The t_p shifts to a shorter annealing time and E_a increases with increasing organoclay-loading due to the enhanced intermolecular interactions between organoclay and nylon 6 chains.

3.9. Identification of specific clays/nylon 6/CB interactions from thermodynamic analysis

In order to assess these interactions, the heat of immersion measurement was performed on unmodified natural-montmorillonite and organo-montmorillonite. Obviously, a dioctahedral 2:1 type layers the smectite group of minerals are the swelling clay and they carry a permanent negative charge. According to the mineralogical interpretation, swelling montmorillonite readily adsorbs polar molecules such as the water in the interlayer space. It alters the d_{001} spacing [73] and also depends on the nature of exchangeable cations. The type of intermolecular interactions between clay/water is mostly ion–dipole interaction [73]. However, the intermolecular interactions between polymers become more complicated with replacement of interlayer inorganic cations by specific organic cations and also with the chemical modification on the pristine clay surfaces due to the presence of both non-polar (physical) and polar (chemical) interactions. These interactions play important roles for intercalation, exfoliation, and nano-scale dispersion in polymers. This interpretation is in accord with the fact that the determination of specific surface area and surface free energy of clay minerals is difficult. As a result, there are very few reported values available at present [74–76].

Table 4 shows the heat of immersion (ΔH_i) for natural clay and organoclay adsorbed by various non-polar and polar organic probe molecules at room temperature with different polarity (n-octane < formamide < water). We observe that the measured ΔH_i per unit surface area of montmorillonite decreases with adsorbed non-polar n-octane and ΔH_i significantly increases with adsorbed polar organic compounds by the chemical modification of natural clay. The above observation indicates that the quantity of ΔH_i varies in the presence of quaternary ammonium chloride with methyl, tallow, bis-2-hydroxyethyl on unsaturated aliphatic chains associated with increase of d_{001} spacing. The large ΔH_i values for polar organic compounds is attributed to the nature of swelling clay and to the higher penetration ability of smaller polar water molecules into the narrow interlayer space than the larger non-polar n-octane molecules.

Table 5 shows calculated surface free energy of natural clay and organoclay with reported values [18] of nylon 6. The equations and theory for the calculations of surface free energy from ΔH_i were used from the corresponding reference [76]. The reported values [77–79] of the surface free energy at room temperature as well as the temperature coefficients for various non-polar and polar organic probe molecules was used for the calculations. The data indicate that London dispersion component of surface tension in organically modified clay is two times larger than that of the natural clay. This result indicates that the chemical modification of clay not only enhances the affinity between polar molecules but also varies the quality of interactions between non-polar molecules. Unfortunately, we were not able to obtain the polar component of surface tension due to the unusually large values of measured ΔH_i for adsorbed polar organic compounds in the swelling clay.

Table 6 shows London dispersion force contributions to interfacial tension (K^d) and work of adhesion (W_a^d) at various

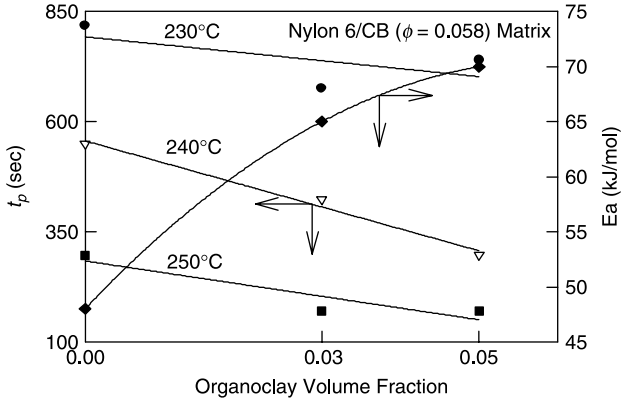

Fig. 19. Plots of t_p versus organoclay volume fraction at various annealing temperatures (left axis) and plots of E_a versus organoclay volume fraction (right axis) for nylon 6/CB ($\phi = 0.058$) system.

Table 4
Heat of immersion (ΔH_i) for various layered silicates adsorbed by various low-molecular-weight probes

Layered silicate	Particle size (μ by volume)[a]	ΔH_i (mJ/m^2)[b]		
		n-Octane C_8H_{18}	Formamide $HCONH_2$	Water H_2O
Cloisite Na^+	2	−102.1	−2229.0	−3158.0
Cloisite 30B	2	−169	−1282.0	−821.0

[a] Data obtained from manufacturer.
[b] Determined from isothermal microcalorimeter at 25 °C.

layered silicates/nylon 6 interface, where the polar component of surface tension is neglected. The geometric-mean equation is used to obtain K^d and it is normally accepted between a low-energy material and a high-energy material [81,82].

$$K = \gamma_1 + \gamma_2 - 2(\gamma_1^d \gamma_2^d)^{1/2} - 2(\gamma_1^p \gamma_1^p)^{1/2} \quad (6)$$

Here, γ_1, γ_2 are the surface tension of phase 1 and phase 2, d denotes the London dispersion component (non-polar), and p denotes the polar component (such as including dipole–dipole, dipole–induced dipole, and hydrogen bonding). When the polar interaction is neglected, Eq. (6) becomes

$$K^d = \gamma_1 + \gamma_2 - 2(\gamma_1^d \gamma_2^d)^{1/2} \quad (7)$$

which is proposed by Fowkes [79]. Similarly, the dispersion component of the W_a^d is defined as

$$W_a^d = 2(\gamma_1^d \gamma_2^d)^{1/2} \quad (8)$$

With the chemical modification of natural clay (Table 6): (i) BET specific surface area of silicate layer decreases roughly 1.4 times and d_{001} spacing of the interlayer increases roughly 1.6 times due to the presence of aliphatic chains of the organic modifier, (ii) K^d increases roughly 5.2 times. We attribute this to the enhancement of London dispersion forces and it allows nylon 6 chains to penetrate into the interlayer spaces, and (iii) W_a^d increases roughly 1.5 times. This is due to the increase in affinity (London interaction) between the positively charged amine end-groups of nylon 6 chains and the negatively charged unmodified pristine clay surfaces [44,82–84], where the nylon 6 chains could directly contact through London (non-polar) interaction. Since, two hydroxyl groups are attached to the unsaturated aliphatic chains of organic modifier on this particular organoclay (Cloisite 30B®), the overall organoclay/nylon 6 interactions by using conventional melt blending are believed to be a combination of weak physical interaction (London) and strong chemical interactions such as hydrogen bonding.

We now offer an explanation on the morphologically observed organoclay/CB 'nano-unit' dispersed in nylon 6 matrix from thermodynamic analysis. Let us consider when an interface between phase 1 and phase 2 is formed spontaneously. The change in free energy is the reversible work of adhesion and this must be zero or negative for the condition of spontaneous separation [80]

$$W_{a,P} = K_{13} + K_{23} - K_{12} \leq 0 \quad (9)$$

where $W_{a,P}$ is the reversible work of adhesion. P denotes that the joint is immersed in a polymer melts (phase 3), K_{ij} is the interfacial tension between phases i and j, where the polar interaction is neglected. Whereas, the condition for thermodynamic stability is given by

$$W_{a,P} = K_{13} + K_{23} - K_{12} > 0 \quad (10)$$

For this analysis, we used the literature value (94.5 mJ/m^2) [18] for the London dispersion component in surface tension for similar low structure CB (Seast 300®). We observe a significant increase of $W_{a,P}$ (58.44 mJ/m^2) in organoclay/nylon 6/CB ternary nano system as compared to $W_{a,P}$ (25.58 mJ/m^2) of natural clay/nylon 6/CB ternary system. The thermodynamic stability is enhanced roughly 2.3 times by the chemical modification. This observation indicates that the large surface area of exfoliated organoclay platelet induces strong nylon 6 chain interactions not only to provide opportunity for nylon 6 chains to be adsorbed through hydrogen bonding (polar interaction) but also through London (non-polar) interaction between the amine-end groups of nylon 6 chains and the negatively charged pristine clay surfaces. CB surface has very small amount of functional groups such as hydroxyl, carboxyl, and carbonyl groups. They are located as disordered-zones between the ordered-zones of small graphitic crystallites in energetically heterogeneous surface areas with sharp edges by small overlapping of graphite-like layers [15,24,85]. This fact indicates that nylon 6 chains prefer to adsorb on the large flat surface of organoclay than the energetically heterogeneous surface of CB. We attribute the kinetics of self-assembly organoclay/CB 'nano-unit' process to the difference in adsorption of nylon 6 chains against organoclay and CB

Table 5
Surface free energy (γ_s) of nylon 6 and various layered silicates at room temperature

Materials	γ_s (mJ/m^2)		
	γ_s^d	γ_s^p	γ_s^{d+p} [a]
Nylon 6	34.6[b]	11.9[b]	46.5[b]
Cloisite Na^+	85.1[c]	–	–
Cloisite 30B	182.0[c]	–	–

[a] γ_s^{d+p} are the surface tension described in two terms: γ_s^d, London dispersion component and γ_s^p, polar component.
[b] Data obtained from Ref. [18].
[c] Data calculated from Eq. (7) of Ref. [76].

Table 6
London dispersion force contributions to interfacial tension (K^d) and work of adhesion (W_a^d) at various layered silicates/nylon 6 interface in room temperature

Clay/nylon 6	Surface area (m^2/g)[a]	d_{001} (nm)[b]	K^d (mJ/m^2)[c]	W_a^d (mJ/m^2)[d]
Cloisite Na^+/nylon 6	12.28	1.17	11.14	108.6
Cloisite 30B/nylon 6	8.62	1.85	57.90	158.6

[a] Determined from surface area analyzer.
[b] Determined from X-ray generator.
[c] Data calculated from Eq. (7) where polar interactions are neglected.
[d] Data calculated from Eq. (8) where polar interactions are neglected.

surfaces. The adsorption energy per unit surface area of organoclay is much larger than CB and nylon 6 chains are just partially entangled on rough CB surfaces.

Fig. 20 shows XRD patterns for nylon 6/CB ($\phi = 0.109$) systems of various 3 vol% clay-loading with bright-field TEM images. The inset shows the low magnification image of Fig. 20(b). The arrow indicates the natural clay tactoids and/or the stacked organoclay platelets. The XRD pattern for 3 vol% organoclay-loading does not show any discernible diffraction peak and it indicates full exfoliation of organoclay as we observe organoclay/CB 'nano-unit' structure from TEM image (Fig. 20(c)). However, the data indicates a large intensity peak at $2\theta = 2.0^\circ$ giving rise to a d_{001} spacing of 85 nm for 3 vol% natural clay-loading and in parallel to this we observe large clay tactoids in TEM images (Fig. 20(b)). This observation suggests that not only natural montmorillonite failed to exfoliate and/or disperse during melt blending but also it failed to induce the mechanism of self-assembly 'nano-unit' structure (advanced percolation phenomenon).

3.10. Proposed mechanism and definition on advanced percolation concept

First, we define advanced percolation concept as: control of carbon black dispersion, percolation behavior and electrical conductivity of polymer–carbon composites while utilizing least amount of carbon black volume fraction.

The mechanism of advanced percolation phenomenon in nylon 6 ternary hybrids is described in (Figs. 21 and 22). These models (the original arts were partially inspired from [85,86]) summarize our current understanding of the advanced percolation phenomenon (Fig. 21). Quantitative analysis of scanning electron microscopy (SEM) images in the absence of organoclay revealed that the CB dispersion is discrete and randomly distributed with no sign of percolation (Fig. 21(a)). 3 vol% organoclay-loading decreases V_f^* from $\phi = 0.155$ to 0.058 that the state of CB dispersion changes from random to aggregated distribution mode Fig. 21(b)). This indicates the presence of organoclay-loading induced network self-assembly at an optimum organoclay concentration. At this low concentration, the presence of large clay platelet walls enhances the entraining process of the CB nanoparticles. The walls only partially interfere in electrical conduction processes (electron hopping through long range contact connectivity of CB) causing a leveling effect on the percolation curves (Fig. 21(b)). When the organoclay-loading is increased to 5 vol% (advances the V_f^* to $\phi = 0.109$), the CB becomes evenly distributed and stabilized throughout nylon 6 matrix due to the significant amount of insulating clay walls and they create too large a statistical barrier in each CB proximity preventing electron transport between CB nanoparticles especially at lower CB volume fractions (Fig. 21(c)). At higher CB volume fractions we also observe tendency to level the percolation curve at 10^{-4}–10^{-6} S cm^{-1} range demonstrating that the significant clay platelet induced CB network formation is still present. It becomes observable at high CB concentrations to overcome the barrier effect of those insulating clay nanoparticle walls.

The driving force for advanced percolation is induced by preferential organoclay–nylon 6 interactions that the nylon 6 chains are forced to adsorb on large flat surface of organoclay during the network formation. The interactions are a combination of weak physical interaction (London

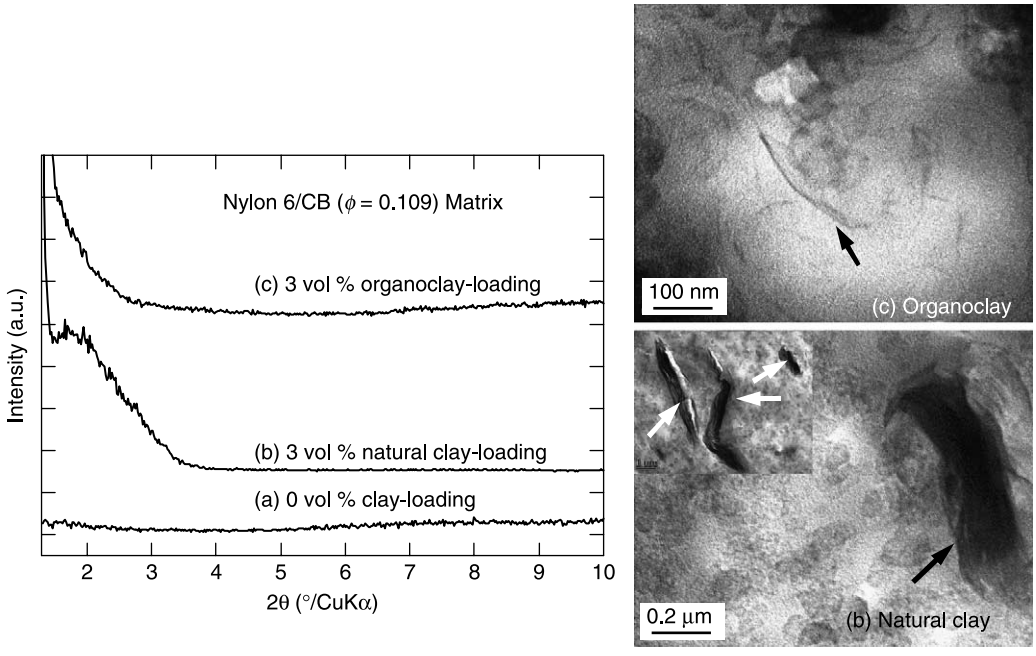

Fig. 20. XRD patterns for various nylon 6/CB ($\phi = 0.109$) systems: (a) 0 vol% clay-loading, (b) 3 vol% natural clay-loading, and (c) 3 vol% organoclay-loading with TEM images, where the inset shows the low magnification image (×9700) of Fig. 21(b), the dark spherical areas represent the primary CB aggregate, and the gray/white areas represent the nylon 6 matrix. The arrow indicates the natural clay tactoids and/or the stacked organoclay platelets (all images are enhanced).

dispersion force) and strong chemical interaction (hydrogen bonding) between the amide group of nylon 6 chains against negatively charged pristine clay and functional groups attached to the organic modifier. The interactions are strong enough to attract CB toward the organoclay platelet, where the end tail side of nylon 6 chains are partially adsorbed and entangled on CB rough surfaces through competitive adsorption against large organoclay flat surfaces (Fig. 22). We must emphasize that at least partially, if possible, fully exfoliated organoclay nano-scale dispersion throughout polymer matrix is essential in order to induce this percolation phenomenon.

We demonstrated that the effective concentration of organoclay optimizes to control of the percolation curve with a consistent electrical conductivity in the narrow intermediate 10^{-6}–10^{-9} S cm^{-1} range. We established the detailed mechanisms of advanced percolation concept as control of CB dispersion, percolation, and electrical conductivity of polymer ternary hybrids by blending dissimilar nanoparticles with conventional polymer processing. These potentially inexpensive high performance materials will be useful for next generation of space and electronic packaging applications in electrostatic discharge protection with precise control of conductivities.

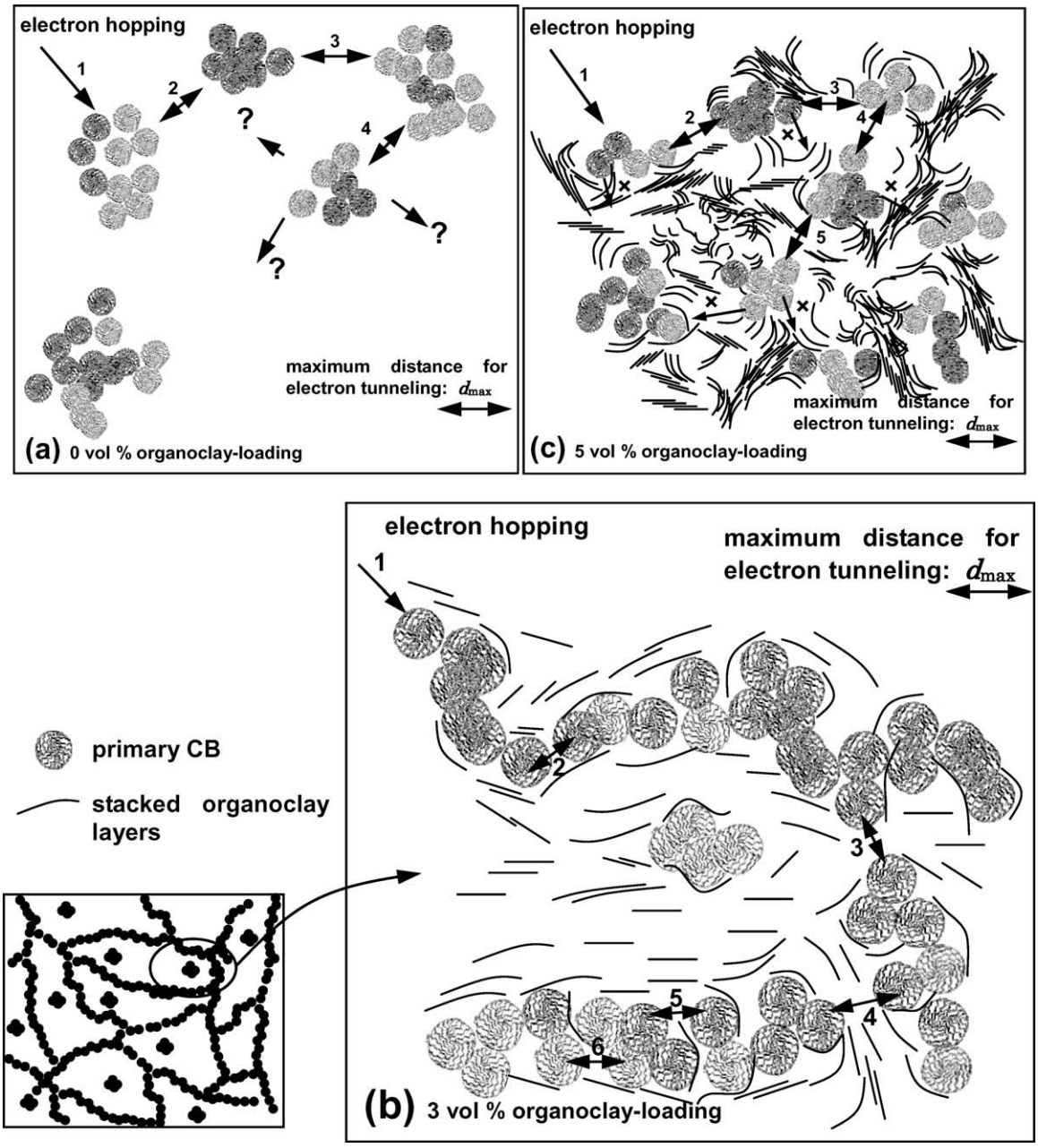

Fig. 21. Schematic of the proposed mechanism of organoclay-loading induced network self-assembly under isothermal zero-shear viscous flow for isotropic nylon 6/CB composites: structural model of 50 dispersed CB particles with (a) 0 vol% organoclay-loading, (b) 3 vol% organoclay-loading, and (c) 5 vol% organoclay-loading.

4. Concluding remarks

Percolation threshold shifts to lower CB volume fractions in the presence of organoclay. With the optimal use of clay nanoplatelet in these systems, we induce nanoplatelet-enhanced self-assembly of CB network facilitating advanced percolation at low CB volume fraction and simultaneously partial blocking the electron hopping pathways to level the slope of percolation curves with a wide range of compositions showing conductivities in the static dissipative range 10^{-6}–10^{-9} S/cm.

The mechanism of this advanced percolation is due to the nature of organoclay/CB 'nano-unit' structure formation. This is a combination of weak physical interaction (London dispersion force) and strong chemical interactions (hydrogen bonding) between the amide group of nylon 6 chains against negatively charged pristine clay and functional groups attached to the organic modifier. This combination of interactions is strong enough to attract CB toward the organoclay platelet, where the end tail sides of nylon 6 chains are partially adsorbed and entangled on CB rough surfaces through competitive adsorption against organoclay large flat surface.

Organoclay can be used as a dispersion control agent in these polymer–carbon systems to induce self-assembly of CB network low CB content, while partially blocking the electron hopping pathways to level the slope of percolation curves. High order exfoliation and nano-scale dispersion of organoclay is essential to induce this advanced percolation phenomenon.

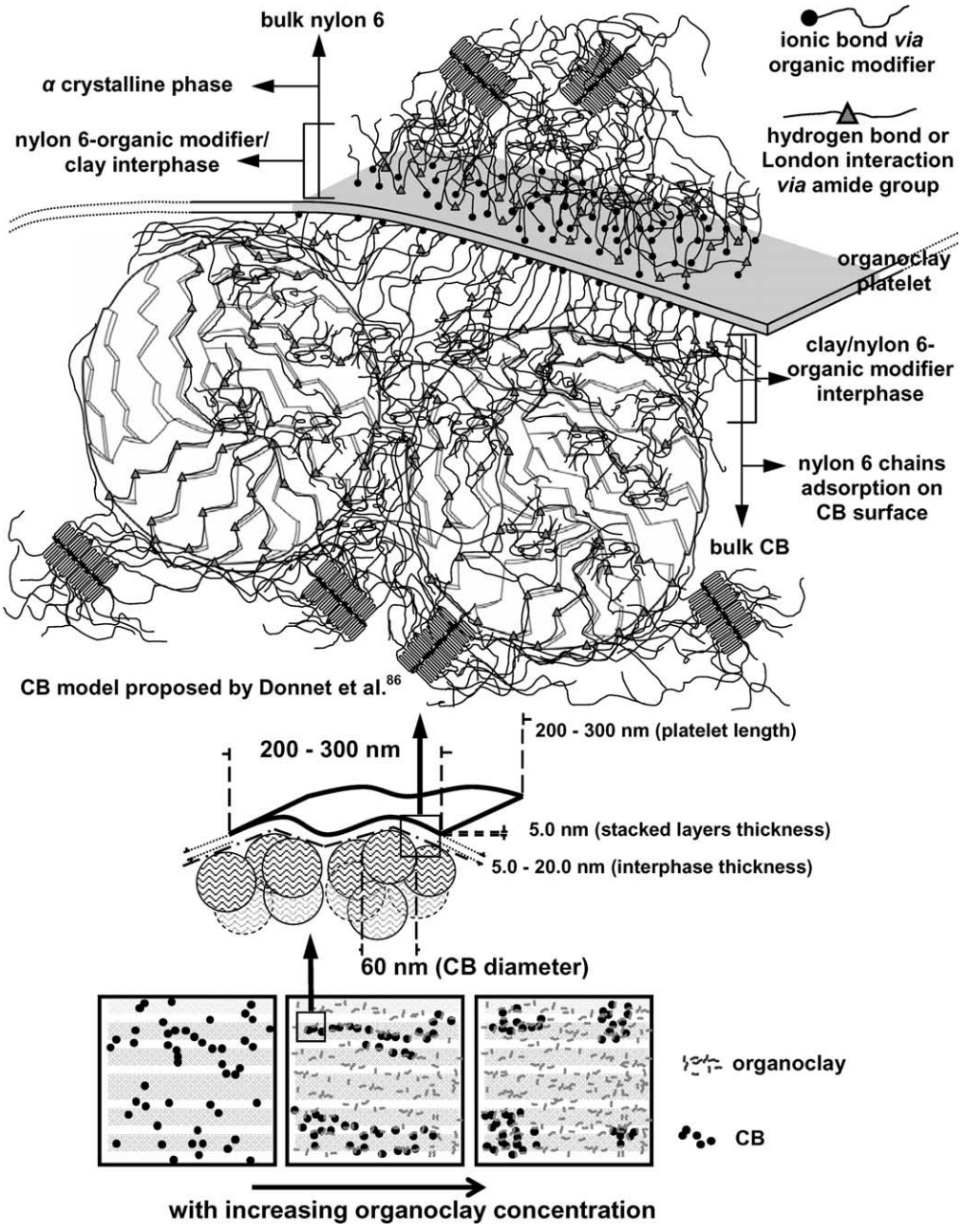

Fig. 22. Schematic of the proposed organoclay/CB 'nano-unit' morphology.

We demonstrated that the effective concentration of organoclay optimizes to control of the percolation curve with a consistent electrical conductivity in the narrow intermediate 10^{-6}–10^{-9} S/cm range.

Acknowledgements

The author thanks Dr M. Sumita, Dr S. Asai and Dr A. Katada of Tokyo Institute of Technology, Dr B. Yalcin and Mr T.L. Kwa of the University of Akron, Dr S. Magonov of Veeco Metrology Group, and Dr M.Y. Pun of Texchem-Pack (M) Bhd. for their fruitful comments and extensive help on experiments.

References

[1] Smith Jr JG, Delozier DM, Connell JW, Watson KA. Polymer 2004;45:613.
[2] Narkis M, Lidor G, Vaxman A. SPE ANTEC Technol Pap 2002;1318.
[3] Flory PJ. Principles of polymer chemistry. Ithaca, NY: Cornell University Press; 1953 [chapter 9].
[4] Stauffer D, Aharony A. Introduction to percolation theory. Washington, DC: Taylor & Francis; 1992.
[5] Gurland J. Trans Met Soc AIME 1966;236:642.
[6] Aharoni SM. J Appl Phys 1972;43:2463.
[7] Janzen J. J Appl Phys 1975;46:966.
[8] Kirkpatrick S. Rev Mod Phys 1973;45:574.
[9] Zallen R. The physics of amorphous solids. New York: Wiley; 1983 [chapter 4].
[10] Bueche F. J Appl Phys 1972;43:4837.
[11] Slupkowski T. Phys Status Solidi A 1984;83:329.
[12] Rajagopal C, Satyam M. J Appl Phys 1978;49:5536.
[13] Yoshida K. J Phys Soc Jpn 1990;59:4087.
[14] Nielsen LE. Ind Eng Chem Fund 1974;13:17.
[15] Donnet JB, Custodero E. Carbon 1992;30(5):81.
[16] Misono S. Nippon Gomu Kyokaishi 1997;70(10):564.
[17] Medalia AI. Rubber Chem Technol 1986;59:432.
[18] Wu G, Asai S, Sumita M, Yui H. Macromolecules 2002;35:945.
[19] Miyasaka K, Watanabe K, Jojima E, Aida H, Sumita M, Ishikawa K. J Mater Sci 1982;17:1610.
[20] Sumita M, Abe H, Kayaki H, Miyasaka K. J Macromol Sci, Phys 1986; B25(1–2):171.
[21] Asai S, Sumita M. J Macromol Sci, Phys 1995;B34(3):28.
[22] Wessling B. Die Makromol Chem 1984;185:1265.
[23] Lux F. J Mater Sci 1993;28:285.
[24] Donnet JB, Voet A. Carbon black. New York: Dekker; 1976.
[25] Sumita M, Sakata K, Asai S, Miyasaka K, Nakagawa H. Polym Bull 1991; 25:265.
[26] Sumita M, Sakata K, Hayakawa S, Asai S, Miyasaka K, Tanemura M. Colloid Polym Sci 1992;270:134.
[27] Gubbels F, Blacher S, Vanlathem E, Jerome R, Deltour R, Brouers F, et al. Macromolecules 1995;28:1559.
[28] Feng J, Chan C-M, Li J-X. Polym Eng Sci 2003;43(5):1058.
[29] Ibarra-Gomez R, Marquez A. Rubber Chem Technol 2003;76:969.
[30] Wu G, Miura T, Asai S, Sumita M. Polymer 2001;42:3271.
[31] Wu G, Asai S, Zhang C, Miura T, Sumita M. J Appl Phys 2000;88(3): 1480.
[32] Wu G, Asai S, Sumita M. Macromolecules 2002;35:1708.
[33] Sumita M, Wu G. Nippon Gomu Kyokaishi 2002;75(9):380.
[34] Foster, JK. Cabot Corporation Technical Report 1990, S-131.
[35] Wu G, Zhang C, Miura T, Asai S, Sumita M. J Appl Polym Sci 2001;80:106.
[36] Katada A, Konishi Y, Isogai T, Tominaga Y, Asai S, Sumita M. J Appl Polym Sci 2003;89:1151.
[37] Sumita M, Asai S, Miyadera N, Jojima E, Miyasaka K. Colloid Polym Sci 1986;264:212.
[38] Zhang MQ, Yu G, Zeng HM, Zhang HB, Hou YH. Macromolecules 1998; 31:6724.
[39] Feller JF, Bruzaud S, Grohens Y. Mater Lett 2004;58:739.
[40] Schueler R, Petermann J, Schulte K, Wentzel HP. J Appl Polym Sci 1997; 63:1741.
[41] Kawasumi M. J Polym Sci, Part A: Polym Chem 2004;42:819.
[42] Okada A, Usuki A. Mater Sci Eng 1995;C3:109.
[43] Mathias LJ, Davis RD, Jarrett WL. Macromolecules 1999;32:7958.
[44] Tanaka G, Goettler LA. Polymer 2002;43:541.
[45] Lee KM, Han CD. Polymer 2003;44:457.
[46] Morishita M. Memoirs of the faculty of science series E, Biology, vol. 2. Fukota, Japan: Kyushu University; 1959 p. 215.
[47] Shimizu Y, Tanemura M, Sumita M, Miyadera N, Miyasaka K. Sen-i Gakkaishi 1986;42:T-261.
[48] Asai S, Kumagaya T, Sumita M, Yui H. Zairyo Kagaku 1997;34(4):190.
[49] Binnig G, Quate C, Gerber C. Phys Rev Lett 1986;56:530.
[50] Shimizu Y, Tanemura M, Sumita M, Miyadera N, Miyasaka K. Sen-i Gakkaishi 1986;42:T-261.
[51] Yerina N, Magonov S. Rubber Chem Technol 2003;76:846.
[52] Viswanathan R, Heaney MB. Phys Rev Lett 1995;75:443.
[53] Van Diemen AJG, Stein HN. J Colloid Interface Sci 1982;86:318.
[54] Brindley GW. In: Brindley GW, Brown G, editors. Crystal structures of clay minerals and their X-ray identification. London: Mineralogical society; 1984 [chapter 2].
[55] Pauling L. Proc Natl Acad Sci, USA 1930;16:578.
[56] Sudo T, Shimoda S, Yotsumoto H, Aita S. Electron micrographs of clay minerals. Tokyo-Amsterdam: Kodansha-Elsevier; 1981.
[57] Solin SA. Annu Rev Mater Sci 1997;27:89.
[58] Oya A, Kurokawa Y, Yasuda H. J Mater Sci 2000;35:1045.
[59] Yalcin B, Cakmak M. Polymer 2004;45:6629.
[60] Yada K. Acta Crystallogr 1967;23:704.
[61] Yada K. Acta Crystallogr 1971;A27:659.
[62] Holmes DR, Bunn CW, Smith DJ. J Polym Sci 1955;17:159.
[63] Arimoto H, Ishibashi M, Hirai M. J Polym Sci, Part A: Polym Chem 1965; 3:317.
[64] Pain R. Reinforcement of elastomers. New York: Interscience; 1975.
[65] Kraus G. J Appl Polym Sci, Polym Symp 1984;39:75.
[66] Nielsen LE, Landel RF. Mechanical properties of polymers and composites. New York: Marcel Dekker; 1976.
[67] Kerner EH. Proc Phys Soc 1956;B69:808.
[68] Wu G, Asai S, Sumita M, Hattori T, Higuchi R, Washiyama J. Colloid Polym Sci 2000;278:220.
[69] Lakdawala K, Salovey R. Polym Eng Sci 1987;27:1035.
[70] Potschke P, Paul DR. Polymer 2002;43:3247.
[71] Wu G, Zheng Q. J Polym Sci, Part B: Polym Phys 2004;42:1199.
[72] Lakdawala K, Salovey R. Polym Eng Sci 1988;28:877.
[73] Khatib K, Francois M, Tekely P, Michot LJ, Bottero JY, Baudin I. J Colloid Interface Sci 1996;183:148.
[74] Budhu M, Giese RF, Van oss CJ. J Geotech Geoenvir Eng 1997;580.
[75] Medout-Marere V, Belarbi H, Thomas P, Morato F, Giuntini JC, Douillard JM. J Colloid Interface Sci 1998;202:139.
[76] Gonzalez-Martin ML, Janczuk B, Labajos-Broncano L, Bruque JM. Langmuir 1997;13:5991.
[77] Jasper JJ. J Phys Chem Ref Data 1972;1:841.
[78] Tsutsumi K, Abe Y. Colloid Polym Sci 1989;267:637.
[79] Fowkes FM. Ind Eng Chem 1964;56(12):40.
[80] Wu S. Polymer interface and adhesion. New York: Marcel Dekker; 1982.
[81] Davis RD, Jarrett WL, Mathias LJ. ACS Symp Ser (Polym Nanocompos) 2002;804:117.
[82] Fornes TD, Hunter DL, Paul DR. Macromolecules 2004;37:179.
[83] Vaia RA, Giannelis EP. Macromolecules 1997;30:7990.
[84] Vaia RA, Giannelis EP. Macromolecules 1997;30:8000.
[85] Leroy P, Revil A. J Colloid Interface Sci 2004;270:371.
[86] Donnet JB. Carbon 1994;32(7):1305.
[87] Fomes TO, Paul DR. Polymer 2003;44:3945.